First High-resolution Observations of Interstellar Pickup Ion Mediated Shocks in the Outer Heliosphere

D. J. McComas[1] , B. L. Shrestha[1] , P. Swaczyna[1] , J. S. Rankin[1] , S. E. Weidner[1], E. J. Zirnstein[1] , H. A. Elliott[2] ,
K. N. Singer[3] , J. Spencer[3], S. A. Stern[3] , and H. A. Weaver[4,5]

[1] Department of Astrophysical Sciences, Princeton University, Princeton, NJ 08544, USA; dmccomas@princeton.edu
[2] Southwest Research Institute, San Antonio, TX 78228, USA
[3] Southwest Research Institute, Boulder, CO 80302, USA
[4] Johns Hopkins University Applied Physics Laboratory, Laurel, MD 20723, USA
Received 2022 May 2; revised 2022 June 11; accepted 2022 June 14; published 2022 August 2

Abstract

This study reports the first high-time-resolution observations of interstellar pickup ions (PUIs) in the outer heliosphere, including the first high-resolution observations of PUIs mediating shocks collected anywhere. These new data were enabled by a clever flight software reprogramming of the Solar Wind Around Pluto (SWAP) instrument on New Horizons to provide ∼30 minutes resolution as compared to the previous ∼24 hr time resolution. This time resolution is sufficient to resolve the shock structures and quantify the particle heating across these shocks. In the ∼10 months of initial data, we observed seven relatively small shocks, including one reverse shock. We find that the PUIs are preferentially compressed and heated across the shocks, indicating compression ratios from ∼1.2–1.8, with little heating for values less than ∼1.5 and progressively more PUI heating for larger compression ratios. In contrast, core solar wind properties did not show consistent changes across the shocks, indicating that these particles (1) participate little in the large-scale fluid-like interactions of the outer heliosphere's combined solar wind and PUI plasma and (2) cannot be used to characterize PUI-mediated shocks as prior studies sought to do. All six forward shock crossings showed gradual increases in PUI pressure over shock widths of ∼0.05–0.13 au, which is roughly three decades larger than characteristic particle scales such as the PUI gyroradii. The new high-resolution observations and results described here are important for understanding shocks in the outer heliosphere, the termination shock, and more broadly for PUI-mediated shocks across many astrophysical systems.

Unified Astronomy Thesaurus concepts: Heliosphere (711); Interplanetary particle acceleration (826); Interplanetary shocks (829); Pickup ions (1239); Solar wind (1534); Space plasmas (1544); Plasma physics (2089)

1. Introduction

The solar wind continuously expands outward from the corona in all directions in space. Its source is spatially and temporally variable, generating solar wind speeds that typically range from ∼300 to 800 km s^{-1} in the inner heliosphere, with even faster flows observed in association with some fast coronal mass ejections (CMEs), especially around solar maximum. Temporal variability of the solar wind and the Sun's rotation cause faster solar wind parcels to align with slower parcels ahead of them. Because the solar wind plasma is magnetized by the interplanetary magnetic field (IMF), the parcels of plasma cannot pass through each other. This interaction makes compressions wherever the faster wind overtakes slower solar wind ahead of it, with some compressions steepening into outward propagating forward shocks. The compressions also produce high-pressure regions that further enhance the forward shocks and can launch reverse shocks back sunward in the solar wind frame (e.g., Burlaga 1974; Gosling et al. 1976; Pizzo 1985; Richter et al. 1985; Smith 1985; Schwenn 1990; Gosling 1997; Richardson 2004).

Many fast–slow solar wind interactions persist over multiple solar rotations, especially around solar minimum, forming corotating interaction regions (CIRs). These CIRs maximize in strength typically around several au and form forward/reverse shock pairs ahead and behind them, respectively (e.g., Hundhausen 1972; Hundhausen & Gosling 1976; Smith & Wolfe 1976; Burlaga 1983; Neugebauer 2013). Farther out in the heliosphere, typically beyond ∼10 au, the CIRs weaken, but they and their shocks can merge together with each other and/or with CMEs and CME-driven shocks, forming merged interaction regions (MIRs). Further out in the heliosphere, these can merge into even larger, globally merged interaction region (GMIR) structures (e.g., Burlaga et al. 1981, 1986, 1997, 2003; Burlaga & Ness 1994; Gazis et al. 1999; Lazarus et al. 1999; Paularena et al. 2001; Richardson et al. 1996, 2002; Richardson & Wang 2005; Richardson 2018). While the difference in speed between the fast and slow parcels continues to wear down with heliospheric distance and the number of shocks is reduced, compression regions should persist, expand, merge, and continue to drive at least some shocks as the residual structures move through the outer heliosphere (Wang & Richardson 2002).

Observations of the core solar wind from the prior Pioneer 10 and Voyager 2 spacecraft (the Voyager 1 solar wind instrument failed around Saturn) showed that from 5 to 20 au—where MIRs typically form and remain strong—shocks were frequent and easy to detect. In this region, ordered and correlated ∼26 day structures were identified via enhanced variations of solar wind density and magnetic field strength. Father out, past ∼30 au, the magnetic field and solar wind density became disordered and uncorrelated,

few shocks were observed (Burlaga et al. 1997, 2003), and the solar wind structures are worn down, reducing the variability of the solar wind in the outer heliosphere (Richardson et al. 1996; Elliott et al. 2016, 2019). Some quasi-periodic structure was present, but only in solar wind speed and temperature outside of the ecliptic plane ($>10°$). These observations showed that a clear change had occurred in the state of the solar wind observable by these spacecraft, somewhere around ~25 au (e.g., Burlaga et al. 1997, 2003; Gazis et al. 1999). Thus, prior observations of the core solar wind made it clear that some critical component is missing from these prior data. This critical and, as of those prior studies, unmeasured component of the solar wind plasma is interstellar pickup ions (PUIs).

Interstellar PUIs are formed when neutral atoms from the very local interstellar medium drift into the heliosphere and become ionized. Once ionized, they are immediately accelerated by the motional electric field of the radially outward moving solar wind. Their injection velocity in the solar wind frame is given by the difference between their velocity and the bulk solar wind velocity in the solar frame. In this electric field, they begin to gyrate about the local IMF, becoming "picked up" and carried away with the bulk solar wind flow. These PUIs undergo rapid pitch angle scattering, leading to transformation of the original ring distribution into a nearly isotropic shell in velocity space. This shell has a broad velocity distribution in the solar frame that varies from near zero up to roughly twice the radially outward solar wind speed. On much longer timescales, PUIs cool in the expanding solar wind and progressively fill in the distribution closer to the solar wind velocity, while newly produced interstellar PUIs join the outermost shell of the distribution.

Interstellar He^+ PUIs were first detected in situ by Möbius et al. (1985). Subsequently, the Solar Wind Ion Composition Spectrometer (SWICS) instrument (Gloeckler et al. 1992) on the ESA/NASA Ulysses mission provided extensive and detailed observations of multiple interstellar PUI species over heliocentric distances from ~1.4 to 5.4 au. These included H^+, He^+, N^+, O^+, and Ne^+ PUIs (Geiss et al. 1994), as well as He^{++} and $^3He^+$ PUIs (Gloeckler et al. 1997). Gloeckler & Geiss (1998) provided a good general review of the Ulysses PUI observations.

Beyond the orbit of Jupiter, McComas et al. (2004) observed the interstellar neutral hydrogen "shadow"—a cavity caused by depletion of interstellar hydrogen for trajectories passing close to the Sun. Those observations were made from the Cassini spacecraft as it transited 6.4–8.2 au, en route to Saturn. Studies of other data from the Pioneer 10 and 11 spacecraft at ~8 au (Intriligator et al. 1996) and 16 au (Mihalov & Gazis 1998) provided only a very limited amount of reprocessed data with "possible signatures" of interstellar hydrogen PUIs.

Finally, with the advent of the Solar Wind Around Pluto (SWAP) instrument (McComas et al. 2008) on the New Horizons mission (see *Space Science Reviews* volume 140, issue 1-4) we have been measuring the detailed distributions and properties of interstellar hydrogen PUIs progressively farther out from the Sun for the first time. SWAP made groundbreaking measurements of the solar wind interaction with Jupiter (McComas et al. 2007, 2017a; Ebert et al. 2010; Nicolaou et al. 2014, 2015a, 2015b) and with Pluto (Bagenal et al. 2016; McComas et al. 2016; Zirnstein et al. 2016), which was its primary mission goal. In the outer heliosphere the innovative design of SWAP (McComas et al. 2008), with very high sensitivity and a large field of view, has further enabled

the simultaneous measurement of the core solar wind (Elliott et al. 2016, 2018, 2019) and hydrogen PUIs (McComas et al. 2010, 2017b, 2021; Randol et al. 2012, 2013; Zirnstein et al. 2018; Swaczyna et al. 2019, 2020).

For the first six years of the New Horizons mission, SWAP was only allowed to be on for brief intervals during spacecraft contacts. This led to only short and sporadic PUI observations between 8 and 22 au (McComas et al. 2010; Randol et al. 2012, 2013). Then, starting in 2012, we implemented a new "hibernation" mode that enabled SWAP to stay on between Earth contacts. This change has allowed the SWAP team to provide an excellent and nearly continuous set of solar wind and hydrogen PUI observations starting at ~22 au and extending out now to beyond 50 au.

McComas et al. (2017b) provided the first major study of these nearly continuous SWAP observations from ~22–38 au. These authors showed that by 20 au, PUIs were already the dominant internal pressure in the solar wind. This result had been predicted theoretically by various authors (e.g., Fahr & Fichtner 1995; Lee 1999; Fahr & Scherer 2005) but not observed before. The pickup process transfers momentum and energy from the bulk motion of the solar wind flow into the PUIs. Elliott et al. (2019) examined the SWAP solar wind observations in comparison to contemporaneous 1 au data and found a 5%–7% reduction in solar wind speed in data from 30–43 au, which is consistent with PUI mass loading. McComas et al. (2017b) also first identified enhanced "tails" above the PUI cutoff and associated them with traveling interplanetary shocks or compressions. Unfortunately, because a magnetometer was not included in the New Horizons payload, it is not possible to definitively identify shocks. Thus, as in prior studies, we use the term "shock" here to describe any rapid increase in solar wind speed.

In order to obtain quantitative moment-like parameters for the PUI properties, McComas et al. (2017b) fit the measured SWAP distributions with the classic Vasyliunas & Siscoe (1976) theoretical model of PUIs, which includes physically motivated parameters of the local hydrogen ionization rate, β_0, and ionization cavity, λ. McComas et al. showed that while the model fits were generally adequate, these two parameters were usually required to be unphysically large or small in order to provide the lowest reduced χ^2 fits to the data. This indicated that this model did not include all of the physics needed to reproduce the PUI distributions in the outer heliosphere.

The problem with the Vasyliunas & Siscoe (1976) model turned out to be that it did not account for the additional heating of the PUIs and instead describes a distribution that simply cools adiabatically as it propagates outward. Chen et al. (2014) proposed an important extension to the Vasyliunas and Siscoe model that included a cooling index, α, which quantifies a variable cooling rate for PUIs as the solar wind expands. This cooling parameter was incorporated by Swaczyna et al. (2020) into a reanalysis of the ~22–38 au data provided by McComas et al. (2017b), to derive the interstellar hydrogen density. This study showed that the interstellar hydrogen density in the vicinity of the heliosphere is in fact much ($\sim40\%$) larger than the previously accepted "consensus" value (Bzowski et al. 2009). Since PUIs are the main source of energetic neutral atoms (ENAs) in the heliosheath through charge exchange with interstellar hydrogen atoms, this density comes in as the square; this larger value may resolve most of a long-standing problem where prior numerical models underestimate ENA fluxes by

roughly a factor of two (e.g., Zirnstein et al. 2017) compared to those observed by IBEX (McComas et al. 2009a, 2009b). The new value of the interstellar hydrogen density is now consistent with astrophysical observations of the density of the local interstellar medium (Slavin & Frisch 2008).

In the most recent prior study of SWAP observations, McComas et al. (2021) extended the PUI data out to 46.6 au. These authors also significantly expanded and improved the analysis, incorporating the PUI cooling index (Chen et al. 2014; Swaczyna et al. 2020) and resolving the issue of the largely unphysical fit parameters of the Vasyliunas & Siscoe distributions seen in earlier SWAP studies (e.g., McComas et al. 2017b). In these studies, the cooling index, α, is defined by $(v/v_b)^\alpha = r_{pickup}/r$, where v is the local PUI speed at the distance of the measurement r, and v_b is the injection speed at the heliocentric distance where the ion was picked up, r_{pickup}. The new procedure also included PUI losses from re-neutralization by charge exchange with other interstellar atoms.

The new function is thus a generalization of the Vasyliunas & Siscoe equation that accounts for PUI losses and allows for cooling even faster than adiabatic ($\alpha < 3/2$) or additional heating of the distribution ($\alpha > 3/2$):

$$f(\boldsymbol{r}, w) = \frac{\alpha S(\boldsymbol{r}, w)}{4\pi} \frac{\beta_0 r_0^2}{r u_{sw} v_b^3} w^{\alpha-3} n_{H,TS}$$
$$\times \exp\left(-\frac{\lambda}{r} \frac{\theta}{\sin\theta} w^{-\alpha}\right) \Theta(1-w) \qquad (1)$$

where the survival probability of PUIs from their pickup distance to the point of observation is $S(\boldsymbol{r}, w)$, $w = v/v_b$, β_0 is the ionization rate normalized to $r_0 = 1$ au, u_{sw} is the bulk speed of the solar wind in the solar frame, θ is the angle between the radial direction and the direction of interstellar hydrogen inflow, $n_{H,TS}$ is the density of the interstellar neutral hydrogen at the upwind termination shock, λ is the size of the hydrogen ionization cavity, where the interstellar neutral atom density decreases by a factor of e, and Θ is the Heaviside step function.

We note that there is only one bulk speed—the solar wind bulk speed is exactly the same as the PUI bulk speed—since the pickup process effectively couples the two together at the moment each interstellar neutral is ionized and a new PUI is incorporated into the solar wind flow. With the inclusion of the cooling parameter, we no longer need to use the size of the hydrogen ionization cavity as a fitting parameter and instead just use its typical value of 4 au (e.g., Sokół et al. 2019). We note that evolution over the solar cycle changes the cavity size by only ~1 au (Ruciński & Bzowski 1995), which has little effect on the fits at much larger distances from the Sun. In contrast, we still fit the local, and more variable, normalized hydrogen ionization rate for the SWAP data and find that it now mostly falls into the expected physical range of ~2×10^{-7} to ~2×10^{-6} s^{-1} (Swaczyna et al. 2020, Figure 7).

McComas et al. (2021) found that most (>93%) of the day-long averaged PUI distributions beyond 22 au indicate that additional heating has occurred above simple adiabatic cooling of the plasma. These authors went on to derive the radial variations of the PUI properties from ~22 to 47 au and produced both "fiducial" values halfway (45 au) and extrapolated values at a nominal upwind termination shock location of 90 au. The values that they found for just upstream of the termination shock are: $n_{PUI} = (4.1 \pm 0.6) \times 10^{-4}$ cm^{-3}, $T_{PUI} = (5.0 \pm 0.4) \times 10^6$ K, $P_{PUI} = 30 \pm 4$ fPa, $\alpha = 2.9 \pm 0.2$, $n_{PUI}/n_{Total} = 0.24 \pm$ 0.02, $T_{PUI}/T_{SW} = 716 \pm 124$, $P_{PUI}/P_{SW} = 173 \pm 32$, and $P_{PUI}/P_{SW-Dyn} = 0.14 \pm 0.01$. McComas et al. (2021) also showed that the heating was enhanced after the passage of compressional waves and shocks in the solar wind. These authors found that shocks and waves were associated with enhancements in PUI densities and temperatures; however, a superposed epoch analysis showed that the peak in the cooling index did not occur at the speed jumps, but instead followed by roughly a week.

Voyager 2 observations showed that the termination shock did not significantly heat the core solar wind plasma (Richardson et al. 2008). This is generally thought to be explained by the bulk of the heating going preferentially into the PUIs (e.g., Zank et al. 2010), which, as discussed above, the Voyagers cannot measure. PUIs are more easily energized at shocks because they have higher thermal energies than the core solar wind, with some of them directed mostly along instead of perpendicular to the shock. Thus, PUIs act as seed particles for energetic particle populations (e.g., Fisk & Lee 1980; Schwadron et al. 1996; Chalov 2001; Giacalone et al. 2002; Fisk & Gloeckler 2006, 2007, 2008; Chen et al. 2015).

PUIs also mediate the structure of collisionless shocks like the termination shock. For example, Mostafavi et al. (2017, 2018) were able to theoretically produce relatively cold thermal plasma while heating the PUIs and showed how the energetic particles govern the structure of these shocks for most magnetic field orientations. Kumar et al. (2018) used particle-in-cell simulations of PUI kinetics and found that the PUIs may be heated by adiabatic compression of the solar wind ahead of shocks. Further, Zank et al. (2018) developed a general theoretical model that included thermal solar wind, the interplanetary magnetic field, and low-frequency turbulence as well as the PUIs. They found that the PUIs can enhance the preexisting low-frequency turbulence, which further enhances wave scattering of the PUIs and heating of thermal ions. This model generally reproduced the observed nonadiabatic solar wind temperature profile observed by SWAP.

SWAP observations in the outer heliosphere are crucial for understanding PUI-mediated shocks, such as interplanetary shocks in the outer heliosphere and the termination shock. Previous SWAP observations, however, had one-day time resolution, and thus have been generally inadequate to use for this purpose. In the only detailed study of an individual shock with SWAP data to date, Zirnstein et al. (2018) examined a strong shock at ~34 au that fortuitously nearly straddled two of the day-long data samples and was therefore analyzable. These authors found a gradient in the upstream energetic particle pressure as indicated by a progressive decrease in the solar wind speed associated with heating of solar wind protons ahead of the shock. The total energy flux per particle was approximately conserved across the shock, with H$^+$ PUIs heated much more than the solar wind ions. The PUIs also developed a tail downstream of the shock that accounted for ~20% of the total downstream energy flux.

In this new study, we provide the first SWAP observations after a significant upgrade to the flight software uplinked in 2021 that allows us to measure individual solar wind and PUI distributions at ~30 minutes resolution—nearly 50 times faster than the one-day distributions previously collected. Section 2 briefly describes the software upgrade, shows an example of the new observations, and describes the fitting procedure and minor modifications from the McComas et al. (2021) fitting process needed for the higher-time-resolution data. Section 3
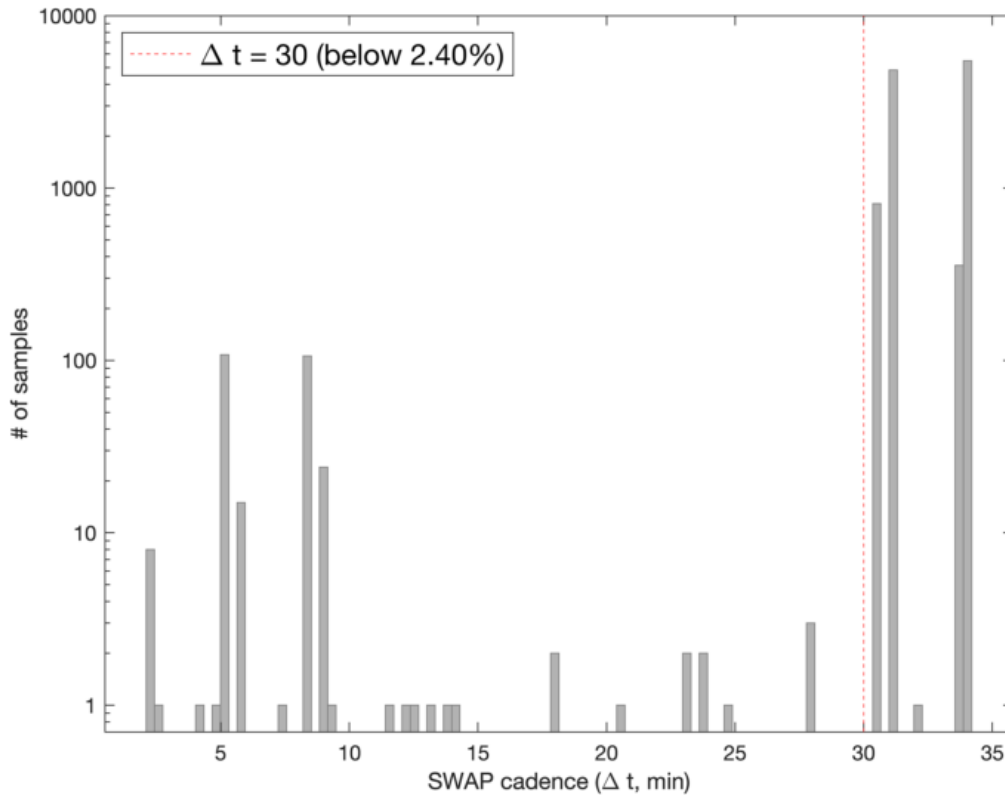
Figure 1. Distribution of 11,777 SWAP sample durations since the upload of the new flight software. We use only samples that are >30 minutes, which comprise 97.6% of all possible data intervals.

shows the full time series of high-resolution SWAP data taken so far and examines in detail the intervals around the seven shocks observed in these high-resolution data. In Section 4, we transform the seven shocks into the their respective moving shock reference frames and examine the effects of the PUI mediation on the shocks. Section 5 explores the implications of these important new observations and analyses. Finally, the Appendix provides more detail about the flight software upgrade and new SWAP instrument sampling procedure. This study documents and serves as the citable reference for the release of these high-time-resolution SWAP observations; these data provide a solid basis for testing detailed theories and models that seek to explain the previously unmeasured physics of PUI-mediated shocks.

2. New High-cadence PUI Observations

The primary SWAP data product is a coarse energy sweep across the full energy range from $\sim35\,\mathrm{eV}/q$ to $\sim7.5\,\mathrm{keV}/q$, followed by a fine energy sweep around the peak of the solar wind found in the prior coarse sweep. This workhorse mode produces both fine and coarse sweeps every 64 seconds. Data from the fine scans further contribute on board to much higher-resolution, but lower-cadence "histogram" data. In early 2018 we identified a simple flight software upgrade that would redefine the internal formatting of a large daily histogram into 47 sequential (~30 minutes) histograms with our normal 64 step energy resolution. This could be done with no change in the overall histogram size or any other external characteristics, and the spacecraft systems would not be affected by this change in any way. Finally, on 2021 February 19, we updated the SWAP flight software aboard New Horizons and started producing this exceptional new data product.

For this study we have a total of 11,777 SWAP samples starting on 2021 February 19 at 18:05:54 UTC, just after the new software was uploaded, and extending through 2021 December 24 at 17:59:31 UTC. While we describe these data as being taken over ~30 minutes, individual samples vary from 2 to 34 minutes. The distribution of individual sample durations is shown in Figure 1. Shorter samples have fewer counts, which have poorer statistics and are not consistent with our use of Gaussian statistics in this analysis. Thus, we reject the 283 samples with less than 30 minutes of data, which reduces the possible data samples by only 2.4%. The mean and median of the remaining samples are 32.56 and 33.64 minutes, respectively.

Another minor enhancement was implemented on 2021 August 9, after SWAP had been off for a few weeks. Based on engineering data, we decided to decrease the maximum voltage on the electrostatic analyzer (ESA) and reduced the maximum analyzed energy from $\sim7.5\,\mathrm{keV}/q$ to $\sim5\,\mathrm{keV}/q$. We then redistributed the top 13 steps to provide finer energy-per-charge resolution in the measurements above $\sim2.5\,\mathrm{keV}/q$. Details of both flight software upgrades are documented in the Appendix, including a table that compares all 64 energy steps.

Figure 2 shows an example of a new ~30 minutes distribution taken on 2021 October 10 at 51.4 au. The SWAP data points are shown by the gray and black dots, along with their 1σ error bars for Poisson counting statistics. The solar wind proton and alpha particle peaks rise well above the PUI distribution, so we fit them with kappa functions (light blue) and subtract them from the distribution. The same is true for the calculated He^+ population, which is produced from the solar wind alpha particles by charge exchange (Swaczyna et al. 2019). We also subtract a constant background (red). Finally,
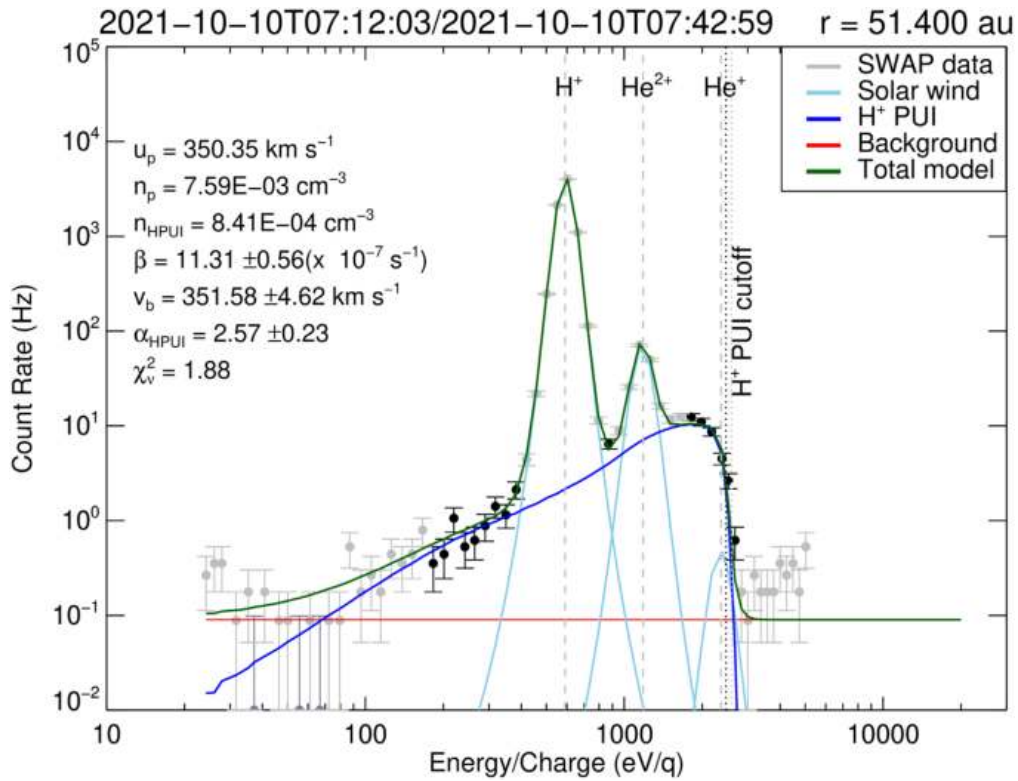
Figure 2. Example of a new, high-cadence, ion distribution (gray and black dots) taken at 51.4 au on 2021 October 10 from 7:12:03 to 7:42:59 UTC. Fits to the solar wind proton (H^+), alpha particle (He^{++}), and He^+ peaks are shown in light blue with centroids indicated by vertical dashed lines. Interstellar H^+ PUIs (dark blue) are fit to the black subset of points using Equation (1) (see text). The solar wind proton speed and density, PUI H^+ density, ionization rate, injection speed, cooling index, and reduced χ^2 for the PUI fit are all listed on the left.

we fit the H^+ PUI distribution (dark blue) to the black subset of data points, which are selected using criteria discussed later in this section (see Figure 2). The PUI points in black that are fit have good signal-to-noise level, especially considering the very short, ∼30 minutes, integration time.

The process for iteratively fitting the E/q spectra at ∼30 minutes resolution is fundamentally the same as we developed previously for fitting 24 hr SWAP spectra (Swaczyna et al. 2020; McComas et al. 2021). However, the counting statistics are roughly 50 times poorer than for the prior day-long samples. These poorer statistics especially affect the low-energy ends and high-energy tails of the distributions. In addition, the distributions are more variable and less "averaged" than for the longer time integrations. These differences meant that we needed to modify and re-optimize the energy bin selection criteria for the fitting procedure. The E/q spectrum from SWAP shown in Figure 1 includes the new PUI distribution fit as indicated by the dark blue curve.

The improvements to the data selection of points to be fit (black data points) required modifications in three areas: (1) below the solar wind proton peak, (2) between the solar wind proton and alpha peaks, and (3) around the proton PUI cutoff. The new criteria were optimized through a series of trial runs and visual inspection of detailed fits in addition to working to minimize the reduced χ^2 values:

1. Below the solar wind proton peak energy, we include all bins down to 30% of the solar wind proton peak energy bin value unless the SWAP count rate in bins is less than twice the modeled solar wind proton count rate.

2. Between the solar wind proton and alpha peaks we have now included a single data point for most of the distributions, including the one shown in Figure 2, because knowledge of the distribution in the middle of the otherwise skipped energy range strongly constrains the PUI fit. We include the bin with the lowest count rate between solar wind proton peak and He^{++} peak unless the SWAP count rate in that bin is less than twice the sum of modeled count rates due to solar wind protons and alpha particles. We note that this procedure fails to find a point for rare samples when the solar wind gets too hot and the proton and alpha distributions broaden.

3. Above the solar wind alpha peak, we accept the five energy bins just below the calculated H^+ PUI cutoff energy. We also always include one energy bin just above this calculated cutoff and any additional consecutive energy bins above the cutoff if their count rate is at least 10% of the maximum count rate between the alpha particle peak and the cutoff. We also remove a small number of single-count data points, which significantly skewed the fits to these distributions.

Finally, the single-count data points are excluded from the analysis, since Gaussian uncertainties used in the χ^2 fitting cannot properly describe the highly asymmetric Poisson distribution corresponding to a single count.

Using the above criteria, we iteratively fit Equation (1) to the remaining black points and minimize the reduced χ^2, following the same procedure as McComas et al. (2021). The only difference is that instead of using solar wind data from the fine

scans for the solar wind parameters (Elliott et al. 2019) as the initial values for the fitting of the solar wind components and calculating the PUI cutoff energy, we use values determined directly from the higher-time-resolution coarse ion spectra. Finally, we reject all data points where the minimized reduced $\chi^2 > 3$. This criterion removes an additional 499 data points, which appear to be largely randomly distributed across the data set and often appear as outliers in various derived solar wind or PUI parameters; five additional obvious single-point outliers were removed manually. This cull plus the earlier removal of time intervals <30 minutes leaves 10,990 samples, or 93.4% of all of the original data points and constitutes the data set used for this study and released for community use with the publication of this paper.

3. PUI-mediated Shocks in the Outer Heliosphere

Figure 3 shows an overview plot of the solar wind and PUI parameters following the process described in Section 2, for the entire interval examined in this study. In these data, we identify seven shocks, as indicated by the vertical lines and sequential numbers. Each shock has a distinct jump in the solar wind speed, although the speed enhancements vary in size with S2 and S6 the largest, S3 and S7 of intermediate size, and S1, S4, and S5 being quite small. We note that compared to shocks in the inner heliosphere, all of these speed jumps are relatively small.

Overall, one can see the stream structure in the density, temperature, and pressure, with compressional increases of various levels at the shocks and decreases in these parameters, along with the solar wind speed, through extended rarefactions after the shocks. However, as shown by McComas et al. (2021), the stream structure correlations are not generally with the core solar wind plasma parameters, as they always are in the inner solar system, but instead with the PUIs. This is because the PUIs contain the vast majority of the internal pressure of the combined solar wind and PUI plasma and thus are the only particles with enough energy to balance the changes in the energy of the bulk motion of the solar wind. We also note that while the solar wind parameters also have relatively large variations, they are of shorter duration and not as obviously associated with the shocks or stream structure.

We now examine each of the seven shock intervals in detail. Figure 4 shows an expanded plot of shock S1, where we see that the shock itself is relatively broad, taking many hours to pass over the spacecraft. Downstream of the shock, the PUIs are heated and compressed, producing a significantly enhanced PUI pressure compared to upstream of the shock. This enhancement is relatively constant and lasts about a week. Another interesting feature is the broad enhancement in the cooling index (α) starting roughly six days after S1. McComas et al. (2021) found a similar broad increase in their superposed epoch analysis, with α peaking about a week after shock passage and taking a couple of weeks to go back to pre-shock values.

In the higher-resolution plot of Figure 4, and the following similar figures for the other shock intervals, we see point-to-point variability in the PUI parameters. This is likely caused by the statistical accuracy of the 30 minutes PUI data and variations in the goodness of their fits. We take the fine-scale PUI parameter variability to be a measure of the accuracy of the parameters derived by our process and thus a likely scale of their full error bars. In contrast, the core solar wind parameters

do not show such point-to-point variability, which makes sense because their fluxes are higher and errors should be lower. However, the solar wind parameters do show large-amplitude, actual structure on shorter timescales than both the (on average) smoother and well correlated variations of the PUI parameters and the combined solar wind and PUI speed.

Figure 5 shows the expanded view of shock S2, which exhibits many of the same features as S1. These include a relatively stable downstream enhancement in PUI density, temperature, and pressure that lasts about a week and an enhancement, albeit smaller, in α around then. This shock appears somewhat narrower in time than S1, but we still clearly resolve the detailed variations of the speed and PUI changes through the shock structure.

Figure 6 shows the expanded view of shock S3. Here, the speed increases in two smaller steps about half a day apart. Increases in the PUI density, temperature, and pressure show a more continuous change, suggesting that they vary on a larger scale than the speed itself. We also note that there is another shock (S4) early on DOY 252 in this plot, but leave that for the next figure to discuss as a separate shock structure.

Figure 7 shows the expanded view of shock S4, which was also visible in Figure 6. This is a very small shock and interestingly, the first not to show an enhancement in α within two weeks after the shock. Shocks S3 and S4 are separated by only ~9 days and, as seen in Figure 3, provide a "double jump" in solar wind speed in the larger structure of solar wind compressions and rarefactions; this could be an example of structures in the process of stacking up on one another and beginning to merge.

Figure 8 shows the expanded view of shock S5, which appears different than the other six shocks. Instead of PUI density, temperature, and pressure going up across the shock, they all decrease. This is the signature of a "reverse" shock, which is propagating back toward the Sun in the outward moving solar wind frame. Also unlike the other shock cases, the solar wind proton density and pressure clearly show a decrease across the shock, but, interestingly, there is a slight increase in temperature.

Unlike the forward shocks in this study, S5 appears as a discontinuous jump rather than a broader, mediated shock structure. This sharper appearance is opposite to what might be expected for observations of the passage of a shock traveling sunward in the solar wind frame across a relatively fixed spacecraft. In addition, S5 is the only shock that shows variations in the core solar wind density, temperature, and pressure consistent with the PUIs and expectations of shock crossings in the inner heliosphere. Thus, we conclude that there may be something intrinsically different about reverse shocks, and PUI mediation of them, compared to forward shocks.

Figure 9 shows the expanded view of shock S6. Similar to the other forward shocks, this shock is somewhat broad and only the PUI parameters consistently increase in the downstream region, although the solar wind pressure does jump up briefly and then back down within the second half of the shock transition itself. Also, once again α is enhanced only after several days post-shock and stays higher for 1–2 weeks.

Finally, Figure 10 shows the expanded view of shock S7, which is similar to the other forward shocks. For this speed increase we also see an enhancement in the solar wind temperature and pressure after the shock, but unlike the PUI density, temperature, and pressure, the solar wind parameters
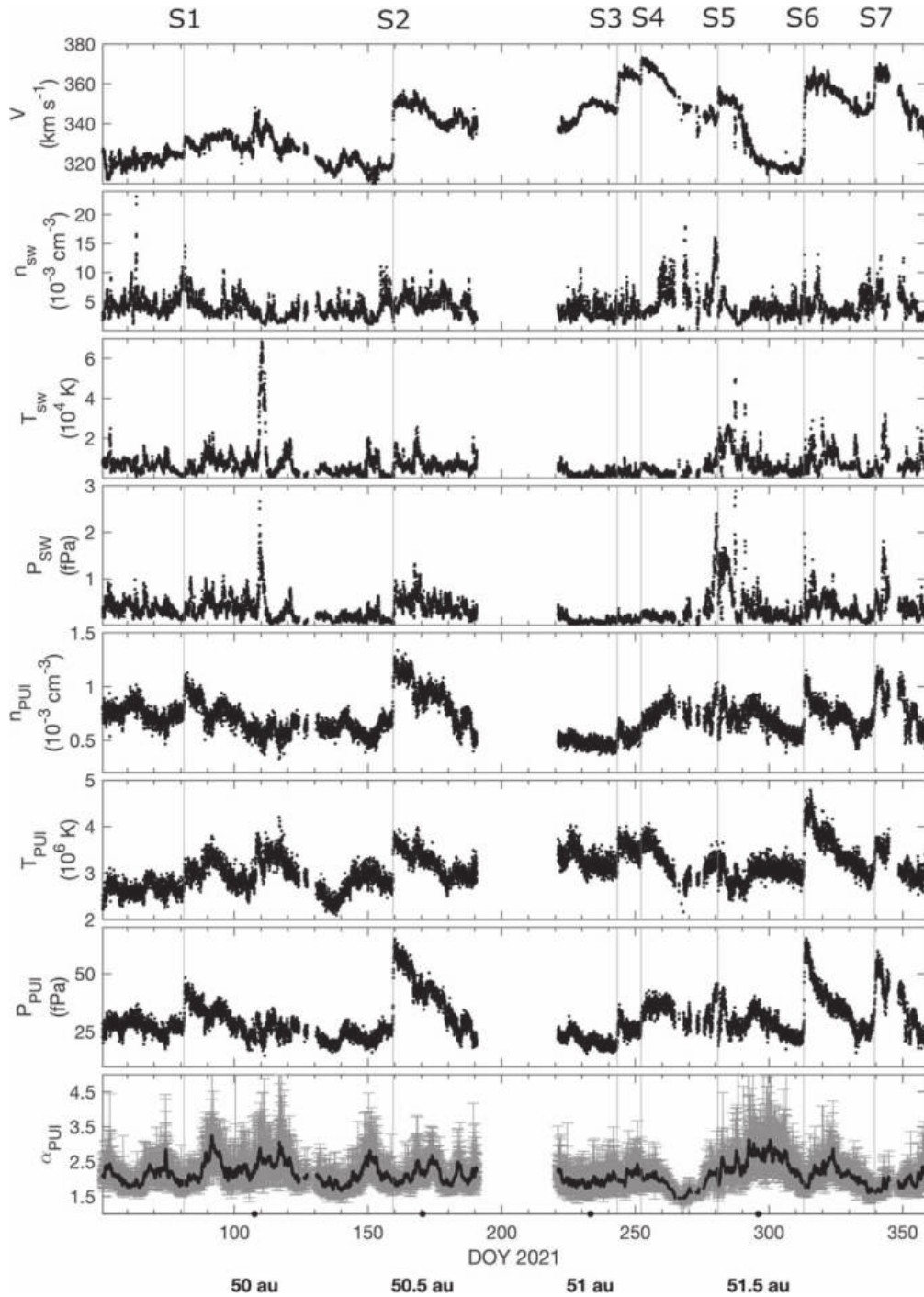
Figure 3. High-resolution SWAP data from 2021 February 19 at 18:05:54 through 2021 December 24 at 17:59:31 UTC. From top to bottom, the panels show bulk speed of the combined solar wind and PUI plasma in the solar frame (spacecraft motion removed); solar wind density, temperature, and pressure (*nkT*); PUI density, temperature, and pressure (*nkT*); and cooling parameter (*α*). Shocks S1–S7 are labeled and identified with vertical lines. Individual cooling parameter samples (bottom panel) are shown in gray and smoothed over running half-day averages (black line).

drop back down after a couple of days and then vary up and down, even though the speed and PUI parameters remain consistently elevated.

Returning to the big picture of these data near and just beyond 50 au (Figure 3), we see the large-scale stream structure of the solar wind with shocks S2, S3/S4, and S7 all creating significant compressions that are followed by long rarefactions. The only clear reverse shock in this interval, S5, is small. Throughout this roughly 10 month interval there are also even smaller jumps in the speed and PUI parameters that we have

not included as shocks in this study owing to the uncertainty of their identifications. As one example, the variations seen in Figure 4 on DOY 89 might be an even smaller reverse shock than S5.

4. Physical Processes in PUI-mediated Shocks

In this section, we examine the seven shocks identified in Section 3 in more detail, using the new high-time-resolution PUI observations in order to better determine the effects of the PUI mediation of these shocks. We begin by converting the
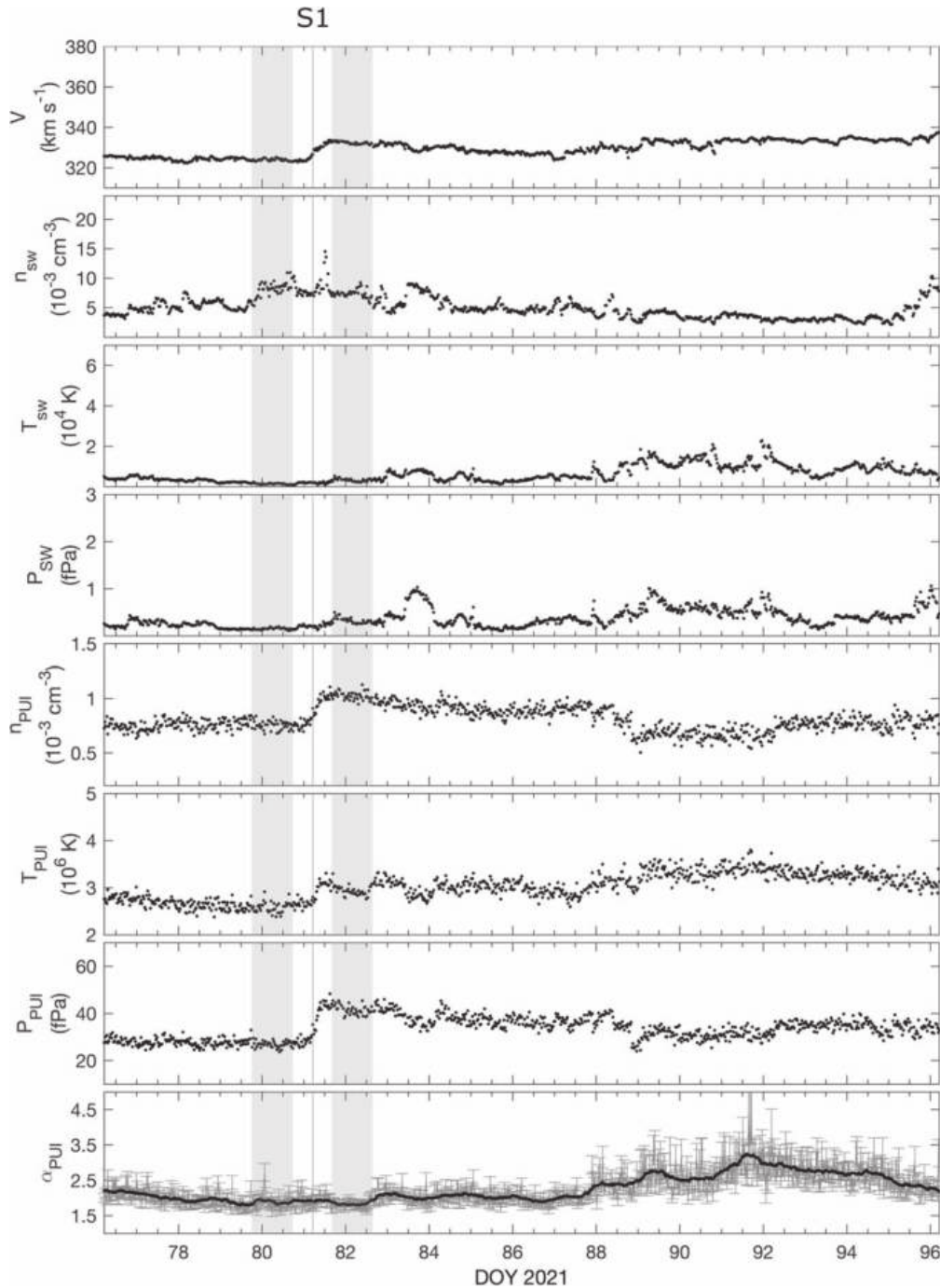
Figure 4. Same panels as in Figure 3, but for a shorter (~20 day) period around shock S1 (vertical line) on 2021 March 22 (DOY 81) at 4:58:42 UTC. The gray shaded areas indicate one-day intervals of relatively stable conditions before and after the shocks, which characterize the upstream and downstream conditions for the large-scale shock transitions; average values in these regions are used in subsequent analysis.

solar wind and PUI data into their moving shock reference frames. To do this, we need to know the shock speed (V_{shock}) in the solar frame. This can be estimated from the measured density and speed in the solar frame upstream (N_u, V_u) and downstream (N_d, V_d), for each shock, respectively. V_{shock} is then $(N_d V_d - N_u V_u)/(N_d - N_u)$. We use the upstream and downstream PUI densities instead of the core solar wind densities since the PUIs provide the dominant pressure, and thus mediate the large-scale shock dynamics.

We use 24 hr of data both before and after the shock as indicated by the gray bars in Figures 4–7 and 9–10, being

mindful to stay away from large-scale variations through the shocks, which appear to be associated with the actual mediated shock structure (note that for the reverse shock, S5, we were only able to find roughly 12 hr before and after with sufficiently stable conditions—see Figure 8—and also that the upstream and downstream sides are reversed in time for S5). This calculation gives shock speeds and compression ratios (N_d/N_u), which we list in Table 1, along with the upstream and downstream parameters used for the calculations for each of the seven shocks and uncertainties calculated as standard deviations of the mean.
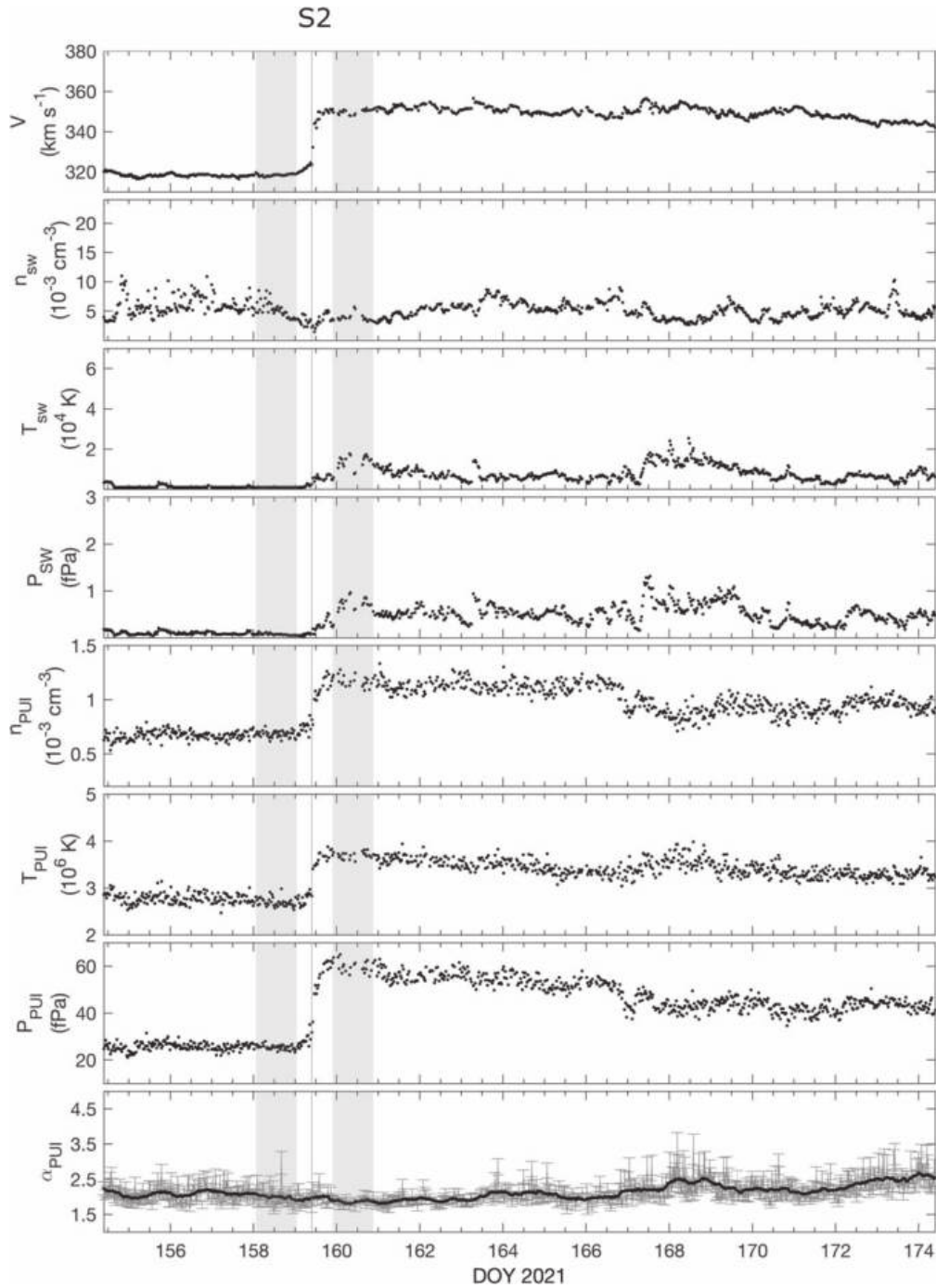
Figure 5. Same as Figure 4, but for shock S2 on 2021 June 8 (DOY 159) at 9:22:11 UTC.

As shown in Table 1, the compression (C-) ratios for the seven shocks studied here range between ∼1.2 and 1.8, which are all relatively weak, especially compared to the strong interplanetary shock observed in late 2015 with the prior 24 hr SWAP PUI measurement cadence (Zirnstein et al. 2018). Following our previous analyses (Zirnstein et al. 2018; McComas et al. 2021), we calculate the energy density flux (hereafter called "energy flux") of the solar wind ions and PUIs for each case in the shock frame. The energy flux for ion species i is a combination of its dynamic energy (first term) and internal energy (second term),

$$E_i = \frac{1}{2}m_i n_i u_s^3 + \frac{\gamma}{\gamma - 1}n_i k_B T_i u_s, \qquad (2)$$

where n_i is number density, T_i is temperature, m_i is mass, u_s is the bulk flow speed in the shock frame, γ is the adiabatic index, and k_B is Boltzmann's constant. We use $\gamma = 5/3$ as Zirnstein et al. (2018) and McComas et al. (2021) did, but note that this value may not be exactly correct, especially near shocks and considering that $\alpha > 3/2$ for the majority of the PUI fits.
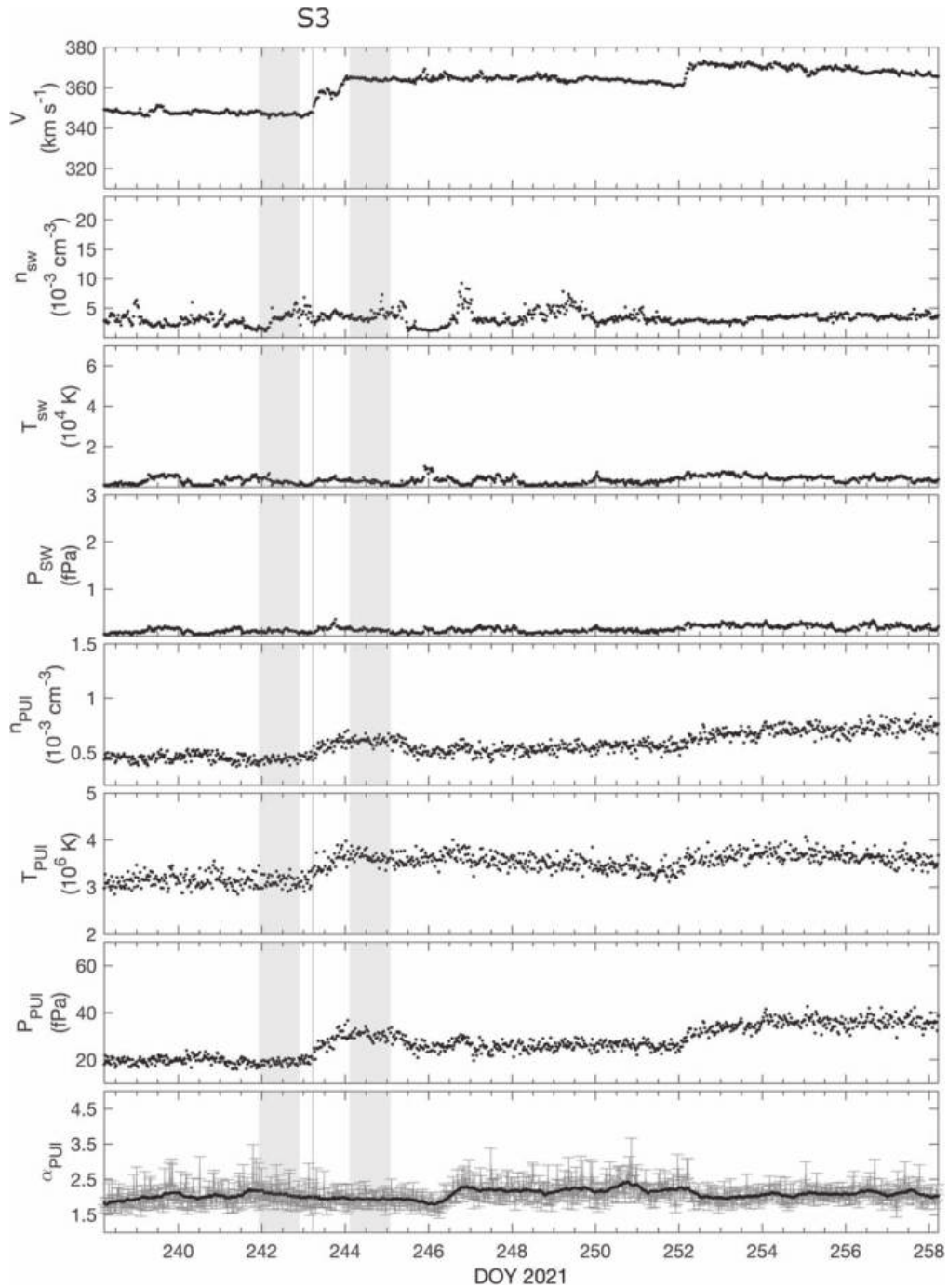
Figure 6. Same as Figure 4, but for shock S3 on 2021 August 31 (DOY 243) at 4:58:43 UTC.

The results of this analysis are presented in Figure 11. In all cases, the energy flux of PUIs exceeds that of the solar wind protons upstream of the shocks (note that S5 is a reverse shock so upstream and downstream are reversed in time). Furthermore, the PUI energy flux increases across the passage of the shocks (between the gray bars) while the solar wind energy flux decreases. This is because the shock is extracting energy from the solar wind flow and converting it (largely) into the PUI population. Thus, the PUIs become even more dominant downstream of the shocks.

While still less than the PUIs, for cases S2, S3, and S6, the solar wind ions have more upstream energy than in the other shocks. The reason for these differences is due to the speed of the shock relative to the solar wind plasma and its compression ratio. The plasma inflow speed in the shock frame is slowest for S1, S4, S5, and S7, and fastest for S2, S3, and S6. The energy flux, shown in Equation (2), is proportional to the sum of dynamic and internal energy density times this bulk flow speed in the shock frame, u_s. For cases where the shock speed is small relative to the bulk flow, the dynamic energy flux of the solar wind ions is small compared to the PUI internal pressure, while for cases when it is large, the solar wind ion dynamic energy flux becomes larger and more similar to the PUI internal pressure. The even stronger shock analyzed by Zirnstein et al. (2018)
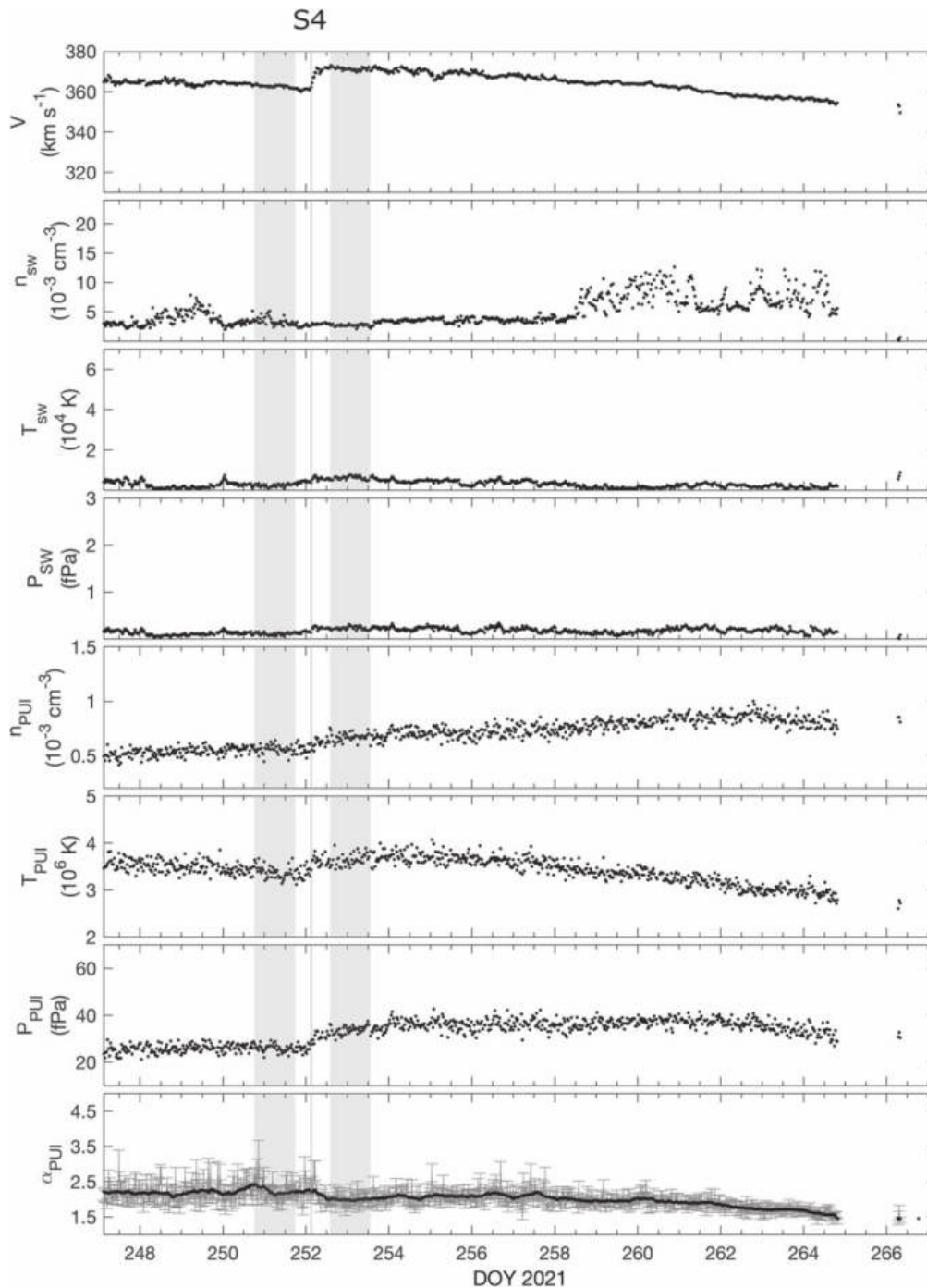
10

Figure 7. Same as Figure 4, but for shock S4 on 2021 September 9 (DOY 252) at 2:48:35 UTC.

had a significantly higher shock speed and compression ratio, and thus an even larger amount of solar wind ion dynamic energy flux upstream of that shock.

Figure 11 only shows the energy flux of the observed solar wind proton and PUI components, but other components should be accounted for when testing for total energy conservation. Zirnstein et al. (2018) found that the magnetic field could hold a non-negligible amount of the energy flux downstream of the strong interplanetary shock observed at ∼34 au from the Sun. Because New Horizons is not equipped with a magnetometer, those authors had to estimate the magnetic field energy upstream and downstream of the shocks. They used a value for the mean magnetic field from ∼25 to

39 au of 0.15 nT based on Voyager observations (Bagenal et al. 2015). For our current study, all shocks are at or beyond ∼50 au so the magnetic field strength is lower on average by about a third and the magnetic energy, which varies as the square of the magnitude, is down to less than half of that for the strong shock at ∼34 au. Because the magnetic field is unmeasured on New Horizons, and is even smaller than in prior, closer-in studies, we do not include it in the energy sums calculated here.

We can, however, estimate the energy flux of alpha particles using SWAP observations of their densities and temperatures and assuming that alpha particles are comoving with the solar wind. Table 2 shows the solar wind proton, alpha particle, and
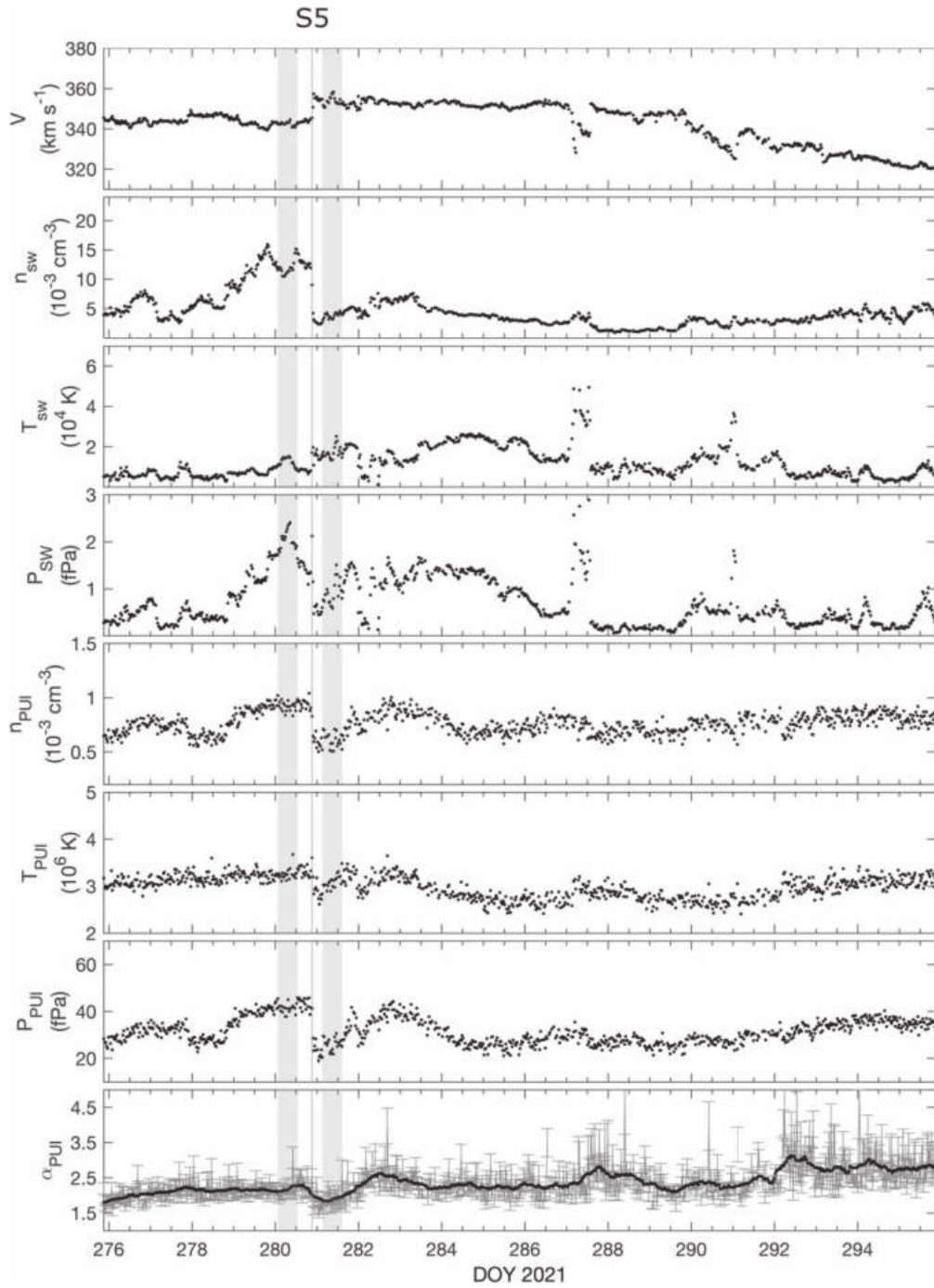
Figure 8. Same as Figure 4, but for shock S5 on 2021 October 10 (DOY 280) at 20:52:19 UTC. Unlike the other six "forward" shocks in this study, S5 is a "reverse" shock, meaning that it is propagating back sunward in the solar wind plasma frame. The gray bars here indicate shorter, half-day averaging intervals before and after this shock as variations in the upstream and downstream parameters were larger. It is interesting to note that the shock jump is extremely narrow in time and the core solar wind as well as the PUI parameters change together, unlike all of the other (forward) shocks in this study.

PUI energy fluxes upstream and downstream of the shocks. The uncertainties in the energy density fluxes are calculated by propagating uncertainties in number density, temperature, and flow speed taken as the standard error of the mean over the shaded regions. Of the three ion components, it is clear that PUIs hold the vast majority (>90%) of the energy flux downstream of all of these shocks.

PUIs preferentially gain energy across quasi-perpendicular shocks in the solar wind due to their large velocity spread in phase space and their ability to gain energy in the upstream motional electric field (e.g., Zank et al. 1996; Chalov & Fahr 2000; Kumar et al. 2018; Yang et al. 2015; Gedalin 2016; Giacalone et al. 2021; Zirnstein et al. 2021). It is expected that, with increasingly stronger shocks, the gain in PUI energy should increase. Figure 12 shows the total (a) and fractional (b) change in energy flux for solar wind and PUIs across the interplanetary shocks presented in this study as a function of compression ratio (circles), as well as the strong interplanetary shock analyzed by Zirnstein et al. (2018) at compression ratio ∼3 (squares).
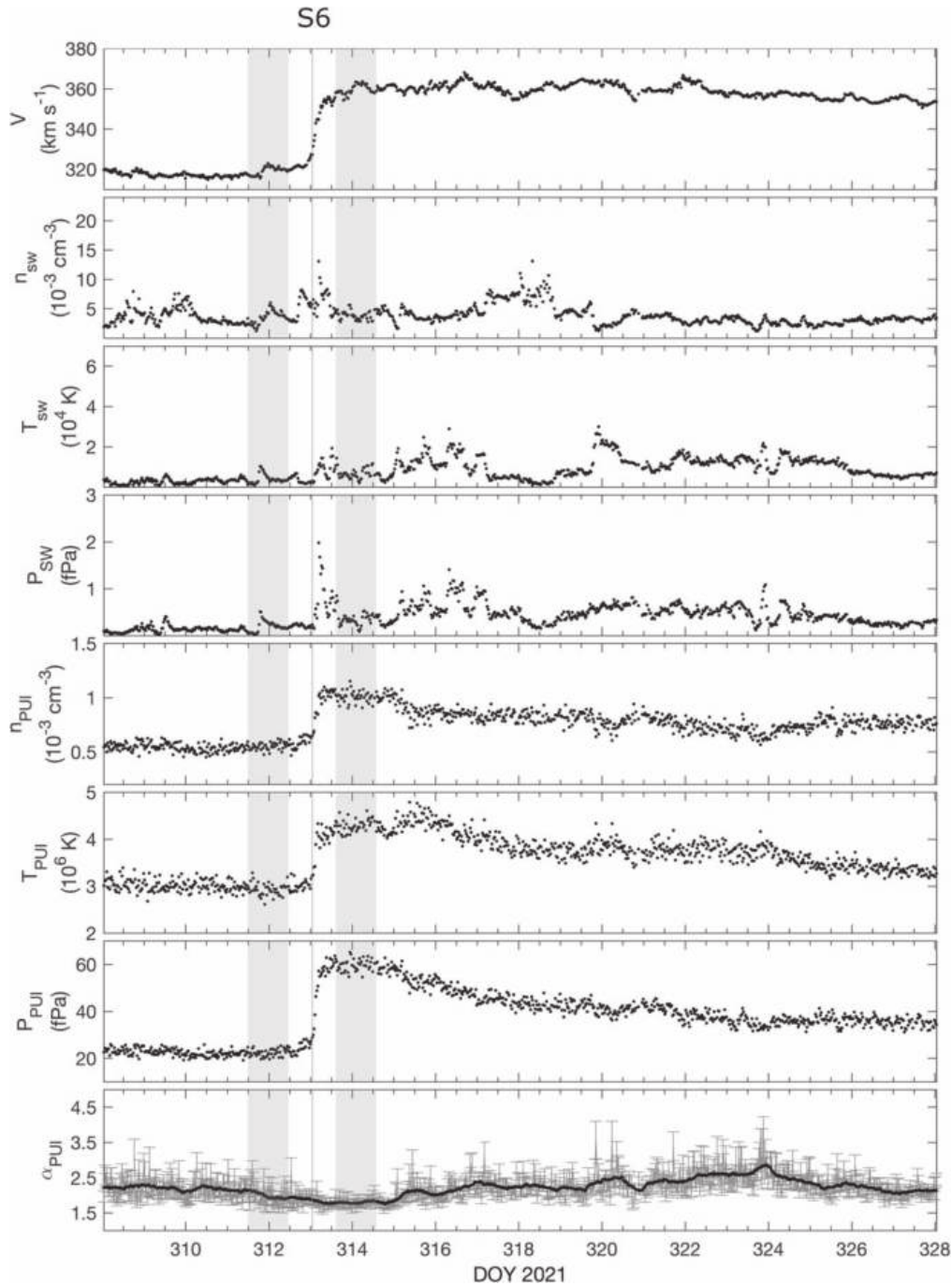
Figure 9. Same as Figure 4, but for shock S6 on 2021 November 9 (DOY 313) at 00:38:27 UTC.

It is clear from Figure 12 that the change in energy is very small for compression ratios below ∼1.5. Above ∼1.5, PUIs gain more energy with increasingly stronger compression ratios. The strongest shock observed in the current study has a compression ratio of ∼1.8, resulting in a gain of ∼2 pPa km s^{-1}, and a loss of energy by a similar amount from bulk motion of the solar wind ions. There is a clear trend of increasing energy gain in PUIs (and energy loss in solar wind ions) for stronger shocks. PUIs increase in energy flux by ∼5%–40% for the cases in this study, and there is nearly a doubling in energy flux for the strong shock observed in late 2015 (squares). Thus, this analysis presents the first observations of preferential PUI shock heating as a function of compression ratio, where

interstellar PUIs dominate the internal pressure of the solar wind and become increasingly more important at mediating shocks with increasing distance from the Sun.

5. Discussion and Conclusions

In this study we examined the first ever high-time-resolution (∼30 minutes) PUI observations in the outer heliosphere. Over roughly 10 months of data in 2021 from ∼49.5 to 52 au, we found seven shocks. Our analysis followed the quantitative procedure of McComas et al. (2021), which includes the PUI cooling index, α, and injection speed fitting. In addition, we made several small modifications to the specific selection of E/q data points in order to optimize the fitting for these much
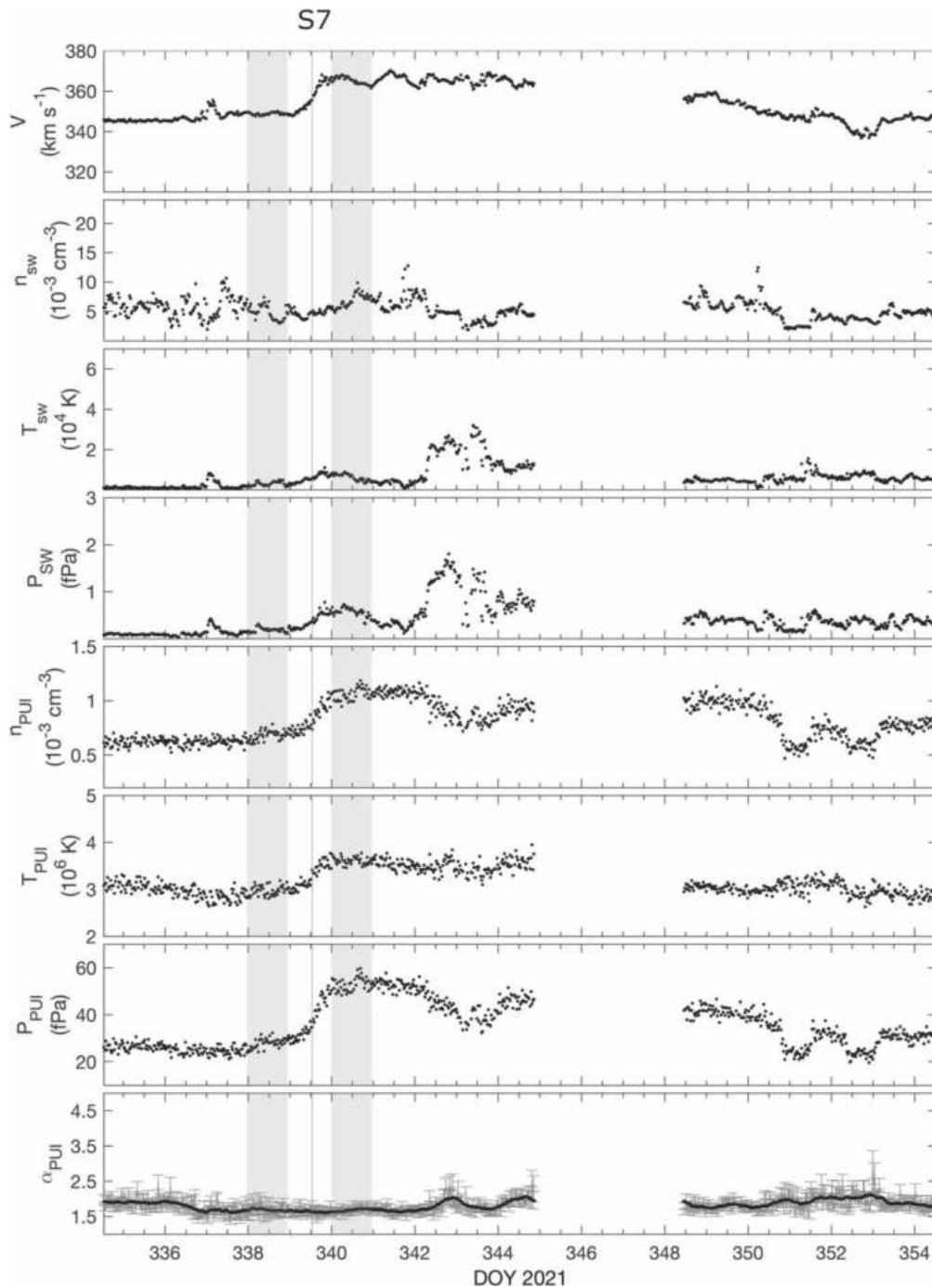
Figure 10. Same as Figure 4, but for shock S7 on 2021 December 5 (DOY 339) at 12:34:11 UTC.

(nearly 50 times) faster, and therefore lower statistics, data. The seven shocks were six forward shocks and one reverse shock, which means that this shock was propagating back toward the Sun in the solar wind frame. We found that the PUI density and temperature both made large-scale changes across all shocks, but the core solar wind parameters largely did not. We also found that the cooling index generally did not increase until one to two weeks after most of the shocks. This delay is similar to, but somewhat longer than, the delay found in the superposed epoch analysis of McComas et al. (2021). Those authors suggested that the delay in the cooling index

enhancement after the passage of a shock could be because the outer shell of the PUI distribution continues to build up from enhanced charge exchange in the higher-density regions downstream of the shocks.

This study showed that all seven shocks preferentially heated the PUIs by extracting energy from the bulk solar wind flow. In contrast, large-scale compression and heating of the core solar wind was not characteristically observed across the shocks, with the solar wind parameters exhibiting erratic small-scale structures and variations sometimes near, but also often away from the shocks. These observations explain the dearth of

Table 1
Upstream and Downstream PUI Parameters and Shock Compression Ratios and Speeds

Shock	DOY 2021	Time (UTC)	Radial Dist. (au)	$N_{\rm u,PUI} \times 10^{-3}$ (cm^{-3})	$N_{\rm d,PUI} \times 10^{-3}$ (cm^{-3})	$V_{\rm u}$ (km s^{-1})	$V_{\rm d}$ (km s^{-1})	C-ratio ($N_{\rm d}/N_{\rm u}$)	$V_{\rm shock}$ (km s^{-1})
1	81	04:58:42	49.79	0.754 ± 0.006	1.026 ± 0.006	323.87 ± 0.09	332.28 ± 0.10	1.36 ± 0.01	355.6 ± 1.0
2	159	09:22:11	50.41	0.682 ± 0.005	1.174 ± 0.011	318.38 ± 0.08	349.91 ± 0.24	1.72 ± 0.02	393.6 ± 1.3
3	243	04:58:43	51.08	0.437 ± 0.004	0.608 ± 0.005	346.83 ± 0.09	364.23 ± 0.09	1.39 ± 0.02	408.5 ± 1.9
4	252	2:48:35	51.15	0.555 ± 0.006	0.672 ± 0.006	362.70 ± 0.09	371.36 ± 0.11	1.21 ± 0.02	412.6 ± 3.4
5	280	20:52:19	51.38	0.606 ± 0.015	0.924 ± 0.011	353.86 ± 0.46	342.43 ± 0.20	1.53 ± 0.04	320.6 ± 2.0
6	313	00:38:27	51.64	0.552 ± 0.005	1.009 ± 0.008	319.24 ± 0.31	359.64 ± 0.39	1.83 ± 0.02	408.6 ± 1.6
7	339	12:34:11	51.85	0.679 ± 0.007	1.062 ± 0.008	348.79 ± 0.10	365.23 ± 0.28	1.57 ± 0.02	394.3 ± 1.3

clearly identifiable shocks—those showing consistent variations of the solar wind parameters—in the outer heliosphere over many decades of prior observations.

Because SWAP is the first instrument capable of measuring PUIs that has flown into the outer heliosphere, it is uniquely capable of making these observations. Now, with the recent reprogramming to provide ~30 minutes data samples, SWAP can resolve these structures and provide detailed measurements across them. It is clear from the seven shocks observed in just the initial ~10 months of data that the compressions from fast CMEs and fast/slow interaction regions, be they CIRs, MIRs, and/or GMIRs, do continue to drive numerous forward and even some reverse shocks in the outer heliosphere beyond 50 au.

We define a "shock transition scale" or characteristic scale length for the large-scale PUI shock transitions. To minimize the effects of single-point variations as discussed above, we take five-sample (~2.5 hr) boxcar averages of the PUI pressure between upstream and downstream regions and determine the distance between the two points in the shock frame where the PUI pressure rises from 15% to 85% of the full pressure jump. The resultant shock transition scales range from 0.05 to 0.13 au with S1: 0.05 au, S2: 0.06 au, S3: 0.13 au, S4: 0.10 au, S6: 0.05 au, and S7: 0.13 au.

Only the reverse shock, S5, is too narrow to resolve with the new SWAP time resolution and instead appears as nearly a step function, with only possibly one sample in transition. With a shock speed in the solar frame of ~320 km s^{-1} and ~30 minutes between samples, we calculate a maximum thickness for S5 of ~600,000 km or just 0.004 au. A reverse shock travels more slowly in the solar frame than an equivalent forward shock since it is propagating back sunward in the solar wind frame, so we might have expected that the shock transition would take longer and appear wider. However, the ~10–30 times narrower thickness of the single reverse shock compared to the six forward shocks sampled so far may thus indicate some fundamental difference in the PUI mediation of forward and reverse shocks.

We compare the shock transition scales to other scale sizes in the plasma. The ion inertial length is the length at which ions decouple from the electrons and can act more as test particles. This length has been associated with shock ramps in plasmas, including at the termination shock (Burlaga et al. 2008). However, this length is only ~3200 km for our typical observed proton densities of ~5 × 10^{-3} cm^{-3}. The gyro-scale sizes for the core solar wind and PUI protons can also be calculated using our typical observed temperatures of ~1 × 10^4 K and 2.8 × 10^6 K, respectively, and a typical magnetic field magnitude of ~0.1 nT, as discussed above. This gives solar wind and PUI gyroradii of ~1200 km and 20,000 km, respectively, the larger of which is

only ~10^{-4} au. Thus, the six forward shock transitions scales are much—three to four orders of magnitude—larger than the ion inertial length or PUI and solar wind proton gyroradii.

We calculate the sonic Mach number of the shock waves, $M_c = u/\sqrt{\gamma\, p/\rho}$, where u is the bulk plasma flow speed in the shock frame, we assume an adiabatic index $\gamma = 5/3$ for all ion species, $p = p_{\rm SWH^+} + p_{\rm SWHe^{++}} + p_{\rm PUIH^+}$ is the total plasma ion pressure, and $\rho = m_{\rm H} n_{\rm SWH^+} + m_{\rm He} n_{\rm SWHe^{++}} + m_{\rm H} n_{\rm PUIH^+}$ is the total mass density. Because the PUI pressure is much larger than the magnetic pressure, the magnetosonic Mach numbers should be only slightly smaller than the sonic Mach numbers. Table 3 compares the sonic Mach numbers upstream and downstream of the shocks. In all cases, the sonic Mach numbers are reduced across the shocks; however, only the two strongest shocks—S2 (compression ratio of 1.72) and S6 (compression ratio of 1.83)—have upstream sonic Mach numbers greater than one. This suggests that the others are not formally shocks and instead that the PUIs have already modified them into PUI-mediated waves. On the other hand, fluid parameters are derived in MHD for Maxwell distributions and not the significantly different PUI distributions, so one should use such values carefully.

All seven shocks studied here are relatively weak, with compression ratios from ~1.2 to 1.8. The energy flux of PUIs is larger than that of the solar wind ions both upstream and downstream of all seven shocks. We find that the upstream flow speed in the shock frame is important because the energy flux (Equation (2)) is proportional to the sum of dynamic and internal energy density times this speed. The dynamic energy flux of the solar wind ions is smaller when the flow speed into the shock is small, and somewhat larger, although still less than the PUI internal pressure, when this flow speed is greater.

We showed here the first observational evidence that the preferential PUI heating is a function of shock strength for compression ratios starting at ~1.5, with little heating below that value. It is interesting that there is little change in energy for compression ratios below this and we note that this may be related to the processes of shock mediation by the PUIs. Theoretical studies of cosmic-ray mediation of, and acceleration at, shocks (e.g., Blandford & Eichler 1987, and references therein) suggest there may be efficient particle acceleration only above a minimum shock compression ratio (e.g., Eichler 1981). These studies were based on significantly higher-energy particles, so their application to the solar wind PUI populations is uncertain. However, the observations in this study are clear: below compression ratios of ~1.5 there is not much heating across the shock, but above this value, the PUI
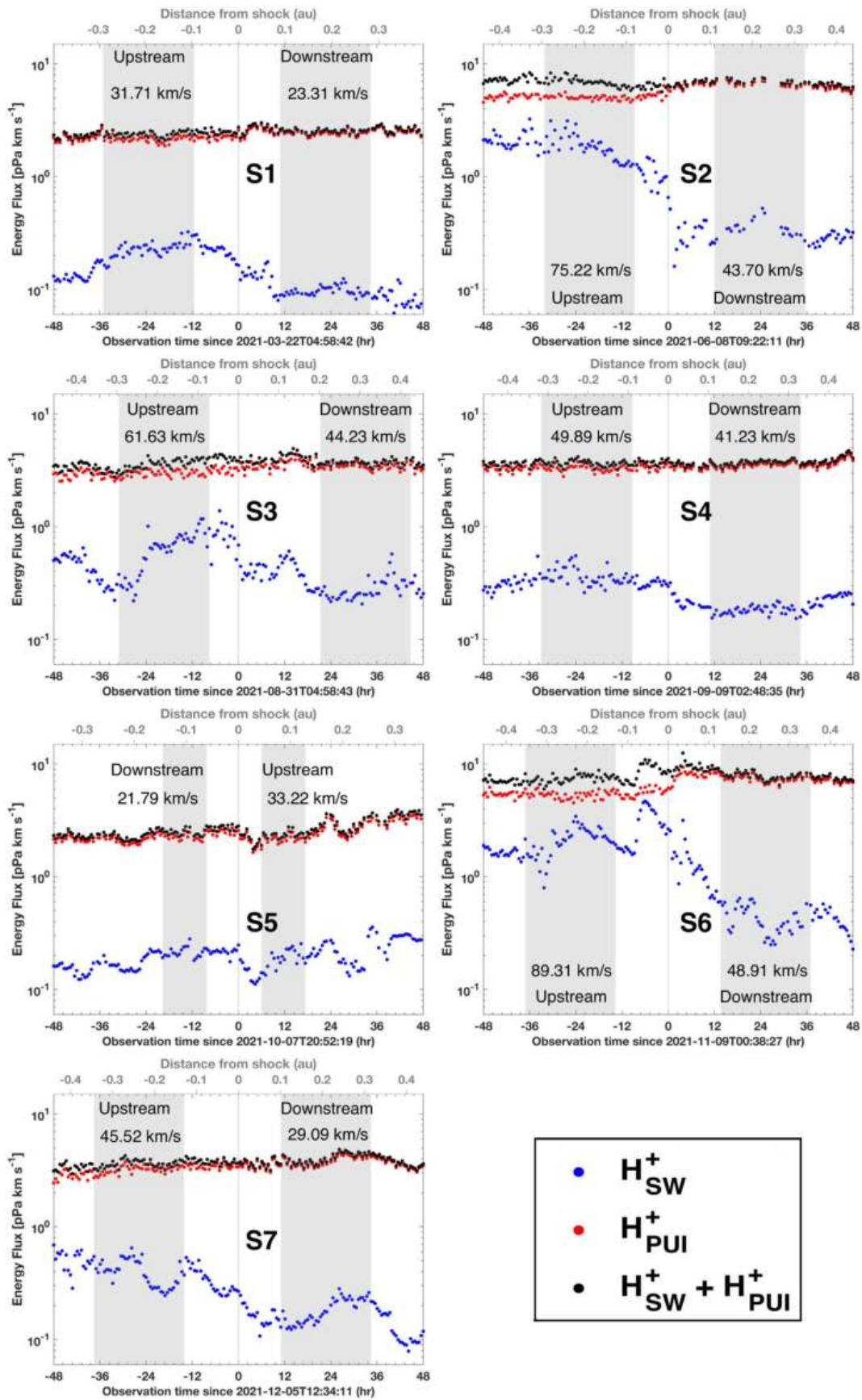
Figure 11. Energy flux of solar wind protons and PUIs observed at the seven shocks (S1–S7) analyzed in this study. The energy flux is calculated using Equation (2), and the calculated bulk flow speeds in the shock frame are listed and used to estimate the distance from the shock shown on the upper *x*-axes. The gray shaded regions indicate data used to calculate the upstream and downstream values shown in Table 1. Note that S5 is a reverse shock so the upstream and downstream sides are reversed.

Table 2
Upstream (u) and Downstream (d) Energy Density Fluxes (EF) in Units of pPa km^{-1} for Solar Wind Protons (SW), PUIs, and Alpha Particles

Shock	$V_{u,shock}$ (km s^{-1})	$V_{d,shock}$ (km s^{-1})	EF$_u$ (SW)	EF$_d$ (SW)	EF$_u$ (PUI)	EF$_d$ (PUI)	EF$_u$ (alpha) [$\times 10^{-1}$]	EF$_d$ (alpha) [$\times 10^{-1}$]	EF$_u$ (SW + PUI + alpha)	EF$_d$ (SW + PUI + alpha)
1	31.7 ± 1.0	23.3 ± 1.0	0.23 ± 0.02	0.10 ± 0.01	2.15 ± 0.07	2.43 ± 0.11	0.07 ± 0.02	0.02 ± 0.01	2.39 ± 0.07	2.53 ± 0.11
2	75.2 ± 1.3	43.7 ± 1.4	1.87 ± 0.15	0.35 ± 0.03	5.02 ± 0.11	6.63 ± 0.23	1.29 ± 0.22	0.46 ± 0.05	7.02 ± 0.19	7.03 ± 0.23
3	61.6 ± 1.9	44.2 ± 1.9	0.65 ± 0.08	0.29 ± 0.04	2.99 ± 0.11	3.42 ± 0.16	0.48 ± 0.05	0.42 ± 0.05	3.67 ± 0.14	3.75 ± 0.17
4	49.9 ± 3.4	41.2 ± 3.4	0.37 ± 0.07	0.18 ± 0.04	3.29 ± 0.24	3.52 ± 0.30	0.92 ± 0.23	0.55 ± 0.11	3.74 ± 0.25	3.76 ± 0.30
5	33.2 ± 2.1	21.8 ± 2.0	0.19 ± 0.03	0.22 ± 0.04	2.16 ± 0.16	2.27 ± 0.22	0.51 ± 0.11	0.05 ± 0.01	2.40 ± 0.16	2.49 ± 0.22
6	89.3 ± 1.7	48.9 ± 1.7	2.13 ± 0.18	0.43 ± 0.05	5.33 ± 0.14	7.41 ± 0.28	0.91 ± 0.08	0.59 ± 0.06	7.55 ± 0.23	7.90 ± 0.28
7	45.5 ± 1.3	29.1 ± 1.3	0.40 ± 0.04	0.19 ± 0.02	3.22 ± 0.11	3.87 ± 0.19	0.49 ± 0.06	0.18 ± 0.02	3.68 ± 0.12	4.08 ± 0.19

heating becomes significant and increases progressively with higher compression ratios.

The findings in this study have important implications for the termination shock and other astrophysical shocks beyond our heliosphere. Voyager 2 observations (Richardson et al. 2008) showed that the termination shock was strongly mediated (e.g., Zank et al. 1996, 2010; Mostafavi et al. 2017), consistent with the large PUI fraction reported by McComas et al. (2021). The Voyager 2 termination shock crossing was estimated to have a compression ratio of ~2.4 as it moved outward and ~1.6 as it moved back inward over the Voyager 2 spacecraft (Richardson et al. 2008). However, these compression ratios were based on the relative densities of the core solar wind plasma and not PUIs, which are not measurable by the Voyagers.

As shown in this current study, the solar wind density does not provide accurate compression ratios. In none of the cases documented in this study would the correct compression ratios be calculated based on the solar wind instead of PUI densities. In fact, using the same intervals as in our analysis above, the compression ratios inferred from the solar wind density would be 0.90, 0.74, 1.16, 0.80, 3.20, 1.10, and 1.41 for S1–S7, respectively. These values are quite different from the actual values we calculated above for the large-scale shock transitions, with three even being less than one and the very weak reverse shock of S5 purporting to be the strongest. Thus, we have significant concerns about any calculations of shocks in the outer heliosphere, including those from Voyager 2, that do not include direct observations of the dominant PUI component.

While there does not appear to be a strong correlation between solar wind ion density and speed at the forward shocks, the solar wind ions exhibit significant, small-scale fluctuations throughout the shock transition process (and elsewhere), making it difficult to use solar wind ion measurements to derive shock jump conditions. However, other than the fine-scale scatter likely due to uncertainties in the fitting process (see above), the PUI parameters vary more smoothly and show a clear correlation with jumps in speed at all observed shocks and compressions, therefore making them useful in deriving shock parameters. The lack of significant correlation between solar wind density and speed suggests the possibility that the core solar wind and PUIs may have different bulk velocities at the shocks. In fact, we often observe a somewhat higher PUI cutoff value downstream of the shocks, which could be an indication of a higher bulk speed. On the other hand, this could also be a higher energy cutoff or the beginning of a suprathermal tail due to particle heating and acceleration at the shock, as suggested by McComas et al. (2017b) and Zirnstein et al. (2018). Ion deflection is possible at PUI-mediated, quasi-perpendicular shocks, because ions may

experience drifts away from the shock normal due to deflection by the cross-shock potential or to magnetic deflection (Leroy 1983; Zank et al. 1996; Kumar et al. 2018), which could influence the measurement of solar wind density. With the one-dimensional E/q measurement from SWAP, however, it may be very difficult to differentiate these fundamental processes.

The high-time-resolution SWAP observations show significant temporal structure in the core solar wind parameters, while the PUI parameters are more smoothly varying throughout the interval studied, including ahead of and behind the seven shocks. Such core solar wind structures are found throughout the 10 month data set, and several show at least some sense of pressure balance, with the solar wind density and temperature being anticorrelated; of course, without magnetic field measurements, pressure balance cannot be tested. The fact that these short-duration variations are generally not reflected in the PUIs could not have been observed in SWAP's prior day-long averaged PUI data.

Thus, another important new finding of this study is that there are smaller-scale structures in the core solar wind parameters that the PUIs largely do not participate in, with the PUI parameters being generally more slowly varying, even across the shocks. One possible explanation is that the size scale of such short-duration structures may be too small for the PUIs to fully participate. As shown above, the ion inertial length and solar wind and PUI gyroradii size scales are all much smaller than the distances over which many-hour solar wind variations occur, so it is not the plasma scales that differentiate these structures. Instead, shock transition scales of ~0.05–0.13 au may reflect the shortest scales over which this PUI-dominated plasma can maintain consistent variations. Perhaps this "smoothness" of the PUI properties could be related to their rate of diffusion, especially along the field.

Turbulence also might provide a larger size scale that would allow core solar wind variations to be essentially decoupled from the PUIs and their dominant pressure. Since the magnetic field is unmeasured on New Horizons, we do not know whether turbulent magnetic structures exist on scales large enough to affect the solar wind but not the PUIs. Another thought is that such structures might have been "born" closer into the Sun, where the PUIs were less important, and then progressively more PUIs were simply added to the distribution with increasing distance.

An intriguing possibility suggested by some, but not all, of the shock transitions is that the core solar wind and possibly (unmeasured) magnetic field could be changing on small spatial scales immediately around the shocks. We noted above that solar wind temperature and density sometimes show small-scale structure not present in the PUIs. For shocks S1 and S6
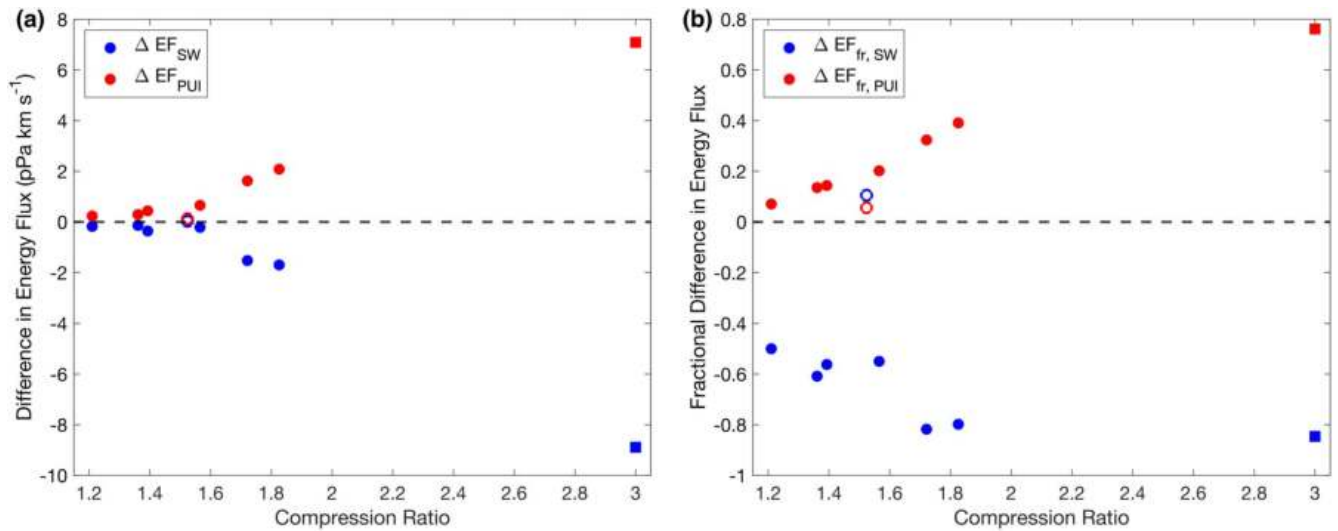
Figure 12. (a) Difference in solar wind (SW) ion and PUI energy flux (in the shock frame) across the shocks as a function of compression ratio. (b) Similar to panel (a), except calculated as the fractional difference in energy flux compared to the upstream values. The seven shocks observed in this study are shown as circles, with open circles showing the reverse shock (S5). We also include the stronger interplanetary shock analyzed by Zirnstein et al. (2018) with much lower time resolution (squares).

Table 3
Sonic Mach Numbers Upstream (1) and Downstream (2) of the Shocks

Shock	M_{c1}	M_{c2}
1	0.59 ± 0.02	0.33 ± 0.01
2	1.18 ± 0.03	0.42 ± 0.01
3	0.88 ± 0.04	0.56 ± 0.04
4	0.68 ± 0.05	0.45 ± 0.04
5	0.43 ± 0.04	0.38 ± 0.02
6	1.23 ± 0.03	0.47 ± 0.02
7	0.70 ± 0.03	0.37 ± 0.02

especially, there are short-duration spikes in solar wind pressure during the second half of the transitions, which quickly go away as the PUI pressure plateaus. Perhaps these lower-energy ions are able to, and do, respond more quickly than the PUI energization required to transfer the energy from the solar wind flow into PUI pressure across the mediated shocks; it is even possible that they represent ions being actively accelerated along the shock.

It is also interesting to consider how much of the observed PUI heating in the distant solar wind can be accounted for simply from the intermittent passage of traveling interplanetary shocks, such as those described in this study. This heating is different than, and in addition to, plasma processing via other physical mechanisms. For example, Zank et al. (2018) suggested that additional heating from the enhanced PUI densities could occur through stochastic acceleration within the ambient and self-generated low-frequency magnetic field turbulence even away from such shocks (e.g., Bogdan et al. 1991; le Roux & Ptuskin 1998; Isenberg 2005; Chalov et al. 2006; Fahr & Fichtner 2011; Gamayunov et al. 2012). While such energization is likely at work in the distant solar wind, it will be important in a future study to quantitatively compare it to the amount of heating from transient shocks and to the level of super-adiabatic heating observed on average through the PUI temperature and α profiles with distance (McComas et al. 2021).

SWAP will continue to take PUI observations at ∼50 times higher time resolution than previously available as the New Horizons spacecraft continues to move outward, roughly toward the nose of the heliosphere, at about 3 au per year. This will enable an even better understanding of the overall variations of PUI properties with radial distance and even more precisely predict the solar wind and PUI properties just upstream of the termination shock. Continuing SWAP observations will further improve our knowledge of these upstream parameters as well as providing many additional PUI-mediated interplanetary shocks to study at ever-increasing heliocentric distances.

Because Voyager 2 could not measure interstellar PUIs, the SWAP observations at traveling interplanetary shocks, such as the ones examined in the study, are the only observational analog available for understanding the physics of the termination shock. Continuing SWAP data will provide high-time-resolution observations of many more forward and even reverse shocks, of varying strengths and geometries. With solar activity increasing, there will be more CMEs and transient events and hopefully we will even sample some much stronger shocks, with compression ratios over 1.8 and possibly even above 3. These observations are the only in situ measurements of PUI-mediated shocks including direct PUI observations. As such, they provide a unique and critical set of observations for understanding such shocks and further test and help us develop our understanding of shock mediation by PUIs generally.

If New Horizons is still operating when it crosses the heliospheric termination shock, SWAP will make critical high-time-resolution PUI observations of that structure for the first time. In the meantime, however, NASA's Interstellar Mapping and Acceleration Probe (IMAP) mission (McComas et al. 2018) will launch in 2025. IMAP is designed to both explore particle acceleration in the solar wind directly and connect it to new and more detailed observations of the outer heliosphere and its interaction with the very local interstellar medium. Continuing SWAP observations through ∼60 au when IMAP launches and beyond will also be helpful in connecting IMAP's in situ data from the Sun–Earth L1 point with its remote

observations of the ENAs generated in the heliosheath from interstellar PUIs that are heated and processed by the termination shock.

More generally, SWAP provides the only data available for directly and experimentally examining PUI-mediated shocks. Such shocks are common across many other astrophysical settings. This makes continuing SWAP observations absolutely essential for developing a general physical understanding of PUI-mediated shocks across the cosmos.

As a final note, this paper provides the detailed information and citable reference for use of the higher-time-resolution (∼30 minutes) SWAP PUI observations starting at 18:05:54 UTC on 2021 February 19, after the new software upload, and extending forward. These important new data, through 17:59:31 UTC on 2021 December 24, are available to the broader scientific community.[6] Owing to the complexities and subtleties of these high-resolution PUI data and the procedures used to correctly analyze them, we urge researchers interested in using these data, or making comparisons to their own theories and models, to reach out to D. J. McComas at dmccomas@princeton.edu.

Appendix
SWAP Flight Software Changes

This appendix documents the two flight software changes that we made on SWAP in 2021. The first software upload occurred on 2021 February 19. This change increased the cadence from daily averages to ∼30 minutes averages (see Figure 1), providing a factor of nearly 50 improvement in the cadence of the SWAP observations.

While the science derived from the SWAP software modification was expected to be significant, the engineering goal of the modification was to have no impact on the spacecraft software or systems, no impact on SWAP data volume, minimal impact on the well proven SWAP flight software, and only minor impact on the science data center processing software on the ground. This approach constrained how we implemented the design change. No new commands or parameters are required to control or operate the daily histogram telemetry. The daily histogram telemetry packets are unchanged in form, size, and frequency; only the contents

Table A1
Nominal Central Energies in eV/q for Each of the 64 SWAP ESA Steps over Time

Bin #	Plan 0 2008-05-28 22:03:46 to 2008-09-28 10:02:34	Plan 2 or 5 2008-09-28 10:02:42 to 2008-10-29 03:04:18	Plan 12a 2008-10-29 03:04:34 to 2021-08-09 00:49:07	Plan 12b Starting from 2021-08-09 00:49:07
1	25.8	22.4	24.2	24.2
2	28.1	24.2	26.1	26.1
3	31.5	27.9	27.9	27.9
4	34.1	29.8	31.6	31.6
5	37.6	33.5	35.3	35.3
6	41.9	35.3	37.2	37.2
7	46.0	39.0	40.8	40.8
8	49.3	42.7	46.4	46.4
9	54.0	48.2	50.1	50.1
10	59.2	51.9	55.6	55.6
11	65.1	57.4	61.1	61.1
12	71.6	63.0	66.7	66.7
13	77.8	68.5	72.2	72.2
14	85.7	75.9	79.5	79.5
15	93.6	83.4	87.0	87.0
16	103	92.5	96.2	96.2
17	113	99.9	105	105
18	124	111	115	115
19	135	120	126	126
20	149	133	139	139
21	163	146	152	152
22	179	159	166	166
23	197	175	183	183
24	215	192	201	201
25	236	210	220	220
26	258	231	242	242
27	283	253	264	264
28	311	277	290	290
29	339	303	318	318
30	372	332	349	349
31	407	364	382	382
32	447	399	419	419
33	492	438	458	458
34	539	480	502	502
35	591	526	550	550
36	644	576	603	603
37	709	631	661	661
38	774	692	725	725
39	848	758	795	795
40	930	832	871	871
41	1018	911	954	954
42	1117	1000	1046	1046
43	1223	1095	1145	1145
44	1341	1201	1256	1256
45	1469	1315	1376	1376
46	1611	1440	1508	1508
47	1767	1578	1654	1654
48	1936	1731	1812	1812
49	1986	1897	1986	1986
50	2175	2078	2175	2175
51	2386	2279	2386	2386
52	2614	2496	2614	2526
53	2870	2741	2870	2678
54	3146	3003	3146	2837
55	3447	3291	3447	3003
56	3777	3607	3777	3181
57	4139	3954	4139	3369
58	4536	4333	4536	3567
59	4972	4748	4972	3777
60	5448	5205	5448	3999

Table A1
(Continued)

Bin #	Plan 0 2008-05-28 22:03:46 to 2008-09-28 10:02:34	Plan 2 or 5 2008-09-28 10:02:42 to 2008-10-29 03:04:18	Plan 12a 2008-10-29 03:04:34 to 2021-08-09 00:49:07	Plan 12b Starting from 2021- 08-09 00:49:07
61	5971	5703	5971	4235
62	6543	6250	6543	4484
63	7171	6850	7171	4748
64	7550	7505	7550	5028

of the data have been changed and one spare bit that was filled with a zero is now set to one as a flag for the changed contents.

The cadence of the new ∼30 minutes average histograms was chosen to fit within the existing histogram data packets framework and the 64 s SWAP acquisition cadence. Within each of the histograms, we nominally sum the counts from 29 coarse sweeps into 64 energy bins. After 29 coarse sweeps have been stored in the histogram, we move on to the next histogram. Periodically, SWAP performs energy sweeps with the deflector turned on. Energy sweeps with deflection are not accumulated into the histogram. These sweeps are apparent in the histogram data because the start time and stop time of the data accumulated are recorded and transmitted for each of the histograms.

Except for the first or last day of accumulating these histograms (in which partial sets will be transmitted) the first 46 histograms of each day have 29 sweeps in them and the last histogram (the 47th) will have fewer. If there had been no deflection sweeps, there would be 16 sweeps in the 47th histogram, but with deflection sweeps subtracted out, that will vary. However, just like start and stop times, all histograms include a count of the total number of sweeps that were accumulated into the histogram, so all of the information necessary for proper analysis is available, and used, on the ground.

The second flight software change occurred on 2021 August 9 after having temporarily suspended operations a couple weeks earlier to double-check the SWAP high-voltage performance. Careful examination of all of the engineering data indicated that we could be approaching the edge of the high-voltage performance, which is not surprising given how long SWAP has been operating in space. Because we essentially never used the top few energy steps, above ∼5 keV for interstellar PUI observations, as we did for the Pluto flyby, we decided to remove these steps and limit the ESA voltages to ∼5 keV instead of ∼7.5 keV. This had the additional advantage of redistributing the energy steps to achieve slightly higher energy-per-charge resolution in the measurements above ∼2.5 keV. The 13 steps were reassigned above this energy to give finer resolution. This resulted in the 64 steps being allocated as described in Plan 12b in Table A1.

ORCID iDs

D. J. McComas ● https://orcid.org/0000-0001-6160-1158
B. L. Shrestha ● https://orcid.org/0000-0002-5247-4107
P. Swaczyna ● https://orcid.org/0000-0002-9033-0809
J. S. Rankin ● https://orcid.org/0000-0002-8111-1444
E. J. Zirnstein ● https://orcid.org/0000-0001-7240-0618
H. A. Elliott ● https://orcid.org/0000-0003-2297-3922
K. N. Singer ● https://orcid.org/0000-0003-3045-8445
S. A. Stern ● https://orcid.org/0000-0001-5018-7537
H. A. Weaver ● https://orcid.org/0000-0003-0951-7762

References

Bagenal, F., Delamere, P. A., Elliott, H. A., et al. 2015, JGRE, 120, 1497
Bagenal, F., Horanyi, M., McComas, D. J., et al. 2016, Sci, 351, aad9045
Blandford, R., & Eichler, D. 1987, PhR, 154, 1
Bogdan, T. J., Lee, M. A., & Schneider, P. 1991, JGR, 96, 161
Burlaga, L. F. 1974, JGR, 79, 3717
Burlaga, L. F. 1983, JGR, 88, 6085
Burlaga, L. F., McDonald, F. B., & Schwenn, R. 1986, JGR, 91, 13331
Burlaga, L. F., & Ness, N. F. 1994, JGR, 99, 19341
Burlaga, L. F., Ness, N. F., Acuna, M. H., et al. 2008, Natur, 454, 75
Burlaga, L. F., Ness, N. F., & Belcher, J. W. 1997, JGR, 102, 4661
Burlaga, L. F., Wang, C., Richardson, J. D., & Ness, N. F. 2003, ApJ, 590, 554
Bzowski, M., Möbius, E., & Tarnopolski, S. 2009, SSRv, 143, 177
Chalov, S. V. 2001, JGR, 106, 18667
Chalov, S. V., Alexashov, D. B., & Fahr, H. J. 2006, ASTRA, 2, 19
Chalov, S. V., & Fahr, H. J. 2000, A&A, 360, 381
Chen, J. H., Bochsler, P., Möbius, E., & Gloeckler, G. 2014, JGRA, 119, 7142
Chen, J. H., Schwadron, N. A., Möbius, E., & Gorby 2015, JGRA, 120, 9269
Ebert, R. W., McComas, D. J., Bagenal, F., et al. 2010, JGR, 115, A12223
Eichler, D. 1981, ApJ, 247, 1089
Elliott, H. A., McComas, D. J., Valek, P., et al. 2016, ApJS, 223, 19
Elliott, H. A., Valek, P., McComas, D. J., et al. 2018, ApJ, 866, 85
Elliott, H. A., McComas, D. J., Zirnstein, E. J., et al. 2019, ApJ, 885, 156
Fahr, H. J., & Fichtner, H. 1995, SoPh, 158, 353
Fahr, H. J., & Fichtner, H. 2011, A&A, 533, A92
Fahr, H. J., & Scherer, K. 2005, JGR, 110, A02103
Fisk, L. A., & Lee, M. A. 1980, ApJ, 237, 620
Fisk, L. A., & Gloeckler, G. 2006, ApJ, 640, L79
Fisk, L. A., & Gloeckler, G. 2007, PNAS, 104, 5749
Fisk, L. A., & Gloeckler, G. 2008, ApJ, 686, 1466
Gamayunov, K. V., Zhang, M., Pogorelov, N. V., Heerikhuisen, J., & Rassoul, H. K. 2012, ApJ, 757, 74
Gazis, P. R., McDonald, F. B., Burger, R. A., et al. 1999, SSRv, 89, 269
Giacalone, J., Jokipii, J. R., & Kóta, J. 2002, ApJ, 573, 845
Giacalone, J., Nakanotani, M., Zank, G. P., et al. 2021, ApJ, 911, 27
Gedalin, M. 2016, JGRA, 121, 10754
Geiss, J., Gloeckler, G., Mall, U., et al. 1994, A&A, 282, 924
Gloeckler, G., & Geiss, J. 1998, SSRv, 86, 127
Gloeckler, G., Geiss, J., Balsiger, H., et al. 1992, A&A, 92, 267
Gloeckler, G., Fisk, L. A., & Geiss, J. 1997, Natur, 386, 374
Gosling, J. T., Hundhausen, A. J., & Bame, S. J. 1976, JGR, 81, 13
Gosling, J. T. 1997, in Coronal Mass Ejections, ed. N. Crooker, J. A. Joselyn, & J. Feynman, Vol. 99 (Washington, DC: AGU), 9
Hundhausen, A. J. 1972, Coronal Expansion and Solar Wind (Berlin: Springer)
Hundhausen, A. J., & Gosling, J. T. 1976, JGR, 81, 1436
Intriligator, D. S., Siscoe, G. L., & Miller, W. D. 1996, GRL, 23, 2128
Isenberg, P. A. 2005, ApJ, 623, 502
Kumar, R., Zirnstein, E. J., & Spitkovsky, A. 2018, ApJ, 860, 156
Lazarus, A. J., Richardson, J. D., Decker, R. B., & McDonald, F. B. 1999, SSRv, 89, 53
le Roux, J. A., & Ptuskin, V. S. 1998, JGR, 103, 4799
Lee, M. A. 1999, Ap&SS, 264, 497
Leroy, M. M. 1983, PhFl, 26, 2742
McComas, D. J., Allegrini, F., Bagenal, F., et al. 2007, Sci, 318, 217
McComas, D. J., Allegrini, F., Bagenal, F., et al. 2008, SSRv, 140, 261
McComas, D. J., Allegrini, F., Bagenal, F., et al. 2017a, JGR, 122, 1763
McComas, D. J., Allegrini, F., Bochsler, P., et al. 2009a, SSRv, 146, 11
McComas, D. J., Allegrini, F., Bochsler, P., et al. 2009b, Sci, 326, 959
McComas, D. J., Elliott, H. A., & Schwadron, N. A. 2010, JGR, 115, A03102
McComas, D. J., Elliott, H. A., Weidner, S., et al. 2016, JGR, 121, 4232
McComas, D. J., Christian, E. R., Schwadron, N. A., et al. 2018, SSRv, 214, 116
McComas, D. J., Schwadron, N. A., Crary, F. J., et al. 2004, JGRA, 109, A02104
McComas, D. J., Swaczyna, P., Szalay, J. R., et al. 2021, ApJS, 254, 19
McComas, D. J., Zirnstein, E. J., Bzowski, M., et al. 2017b, ApJS, 233, 8
Mihalov, J. D., & Gazis, P. R. 1998, GRL, 25, 241
Möbius, E., Hovestadt, D., Klecker, B., et al. 1985, Natur, 318, 426
Mostafavi, P., Zank, G. P., & Webb, G. M. 2017, ApJ, 841, 4

Mostafavi, P., Zank, G. P., & Webb, G. M. 2018, ApJ, 868, 120
Neugebauer, M. 2013, SSRv, 176, 125
Nicolaou, G., McComas, D. J., Bagenal, F., & Elliott, H. A. 2014, JGR, 119, 3463
Nicolaou, G., McComas, D. J., Bagenal, F., et al. 2015a, P&SS, 111, 116
Nicolaou, G., McComas, D. J., Bagenal, F., et al. 2015b, P&SS, 119, 222
Paularena, K. I., Wang, C., von Steiger, R., & Heber, B. 2001, GRL, 28, 2755
Pizzo, V. J. 1985, in Collisionless Shocks in the Heliosphere: Reviews of Current Research, ed. B. Tsurutani & R. G. Stone, Vol. 35 (Washington, DC: AGU), 51
Randol, B. M., McComas, D. J., Gosling, J. T., Elliott, H. A., & Schwadron, N. A. 2012, ApJ, 755, 75
Randol, B. M., McComas, D. J., & Schwadron, N. A. 2013, ApJ, 768, 120
Richardson, J. D., Belcher, J. W., Lazarus, et al. 1996, in AIP Conf. Proc. 382, 8th Int. Solar Wind Conf. (Melville, NY: AIP), 483
Richardson, J., Kasper, J., Wang, C., et al. 2008, Natur, 454, 63
Richardson, I. G. 2004, SSRv, 111, 267
Richardson, I. G. 2018, LRSP, 15, 1
Richardson, J. D., Paularena, K. I., Wang, C., & Burlaga, L. F. 2002, JGR, 107, A4
Richardson, J. D., & Wang, C. 2005, in AIP Conf. Ser. 781, The Physics of Collisionless Shocks: 4th Annual IGPP Int. Astrophysics Conf., ed. G. Li, G. P. Zank, & C. T. Russell (Melville, NY: AIP), 278
Richter, A. K., Hsieh, K. C., Lutrell, et al. 1985, in Collisionless Shocks in the Heliosphere: Reviews of Current Research, ed. B. Tsurutani & R. G. Stone, Vol. 35 (Washington, DC: AGU), 33

Ruciñski, D., & Bzowski, M. 1995, A&A, 296, 248
Schwadron, N. A., Fisk, L. A., & Gloeckler, G. 1996, GeoRL, 23, 2871
Schwenn, R. 1990, in Physics of the Inner Heliosphere, ed. R. Schwenn & E. Marsch (Berlin: Springer), 99
Slavin, J. D., & Frisch, P. C. 2008, A&A, 491, 53
Smith, E. J., & Wolfe, J. H. 1976, GRL, 3, 137
Smith, E. J. 1985, in Collisionless Shocks in the Heliosphere: Reviews of Current Research, ed. B. Tsurutani & R. G. Stone, Vol. 35 (Washington, DC: AGU), doi:10.1029/GM035p0069
Sokoł, J. M., Kubiak, M. A., & Bzowski, M. 2019, ApJ, 879, 24
Swaczyna, P., McComas, D. J., & Zirnstein, E. J. 2019, ApJ, 875, 36
Swaczyna, P., McComas, D. J., Zirnstein, E. J., et al. 2020, ApJ, 903, 48
Vasyliunas, V. M., & Siscoe, G. L. 1976, JGR, 81, 1247
Wang, C., & Richardson, J. D. 2002, GRL, 29, 1181
Yang, Liu, Y, Richardson, J. D., et al. 2015, ApJ, 809, 28
Zank, G. P., Pauls, H. L., Cairns, I. H., & Webb, G. M. 1996, JGR, 101, 457
Zank, G. P., Heerikhuisen, J., Pogorelov, N. V., Burrows, R., & McComas, D. 2010, ApJ, 708, 1092
Zank, G. P., Adhikari, L., Zhao, L.-L., et al. 2018, ApJ, 869, 23
Zirnstein, E. J., Heerikhuisen, J., Zank, G. P., et al. 2017, ApJ, 836, 238
Zirnstein, E. J., Kumar, R., Bandyopadhyay, R., et al. 2021, ApJL, 916, L21
Zirnstein, E. J., McComas, D. J., Elliott, H. A., et al. 2016, ApJL, 823, L30
Zirnstein, E. J., McComas, D. J., Kumar, R., et al. 2018, PhRvL, 121, 075102